Highlights

Sensitivity of boundary layer features to depth-dependent baroclinic pressure gradient and turbulent mixing in an ocean of finite depth

Víctor J. Llorente, Enrique M. Padilla, Manuel Díez-Minguito

- Improved Ekman solutions: variable eddy viscosity and baroclinicity in finite-depths
- Numerical solutions extend previous ones and widens the parameter space explored
- Currents are truly decoupled into geostrophic and ageostrophic terms
- Baroclinicity deflects 45° to the left from the density-gradient direction
- As stratification increases, surface current deflects 45°-90° to the right of wind

Sensitivity of boundary layer features to depth-dependent baroclinic pressure gradient and turbulent mixing in an ocean of finite depth

Víctor J. Llorente[a,b,*], Enrique M. Padilla[c,b], Manuel Díez-Minguito[b]

[a] *University of Zaragoza, C. de Pedro Cerbuna 12, Zaragoza, 50009, Aragon, Spain*
[b] *Andalusian Inter-University Institute for Earth System Research (IISTA), University of Granada, Av. del Mediterraneo s/n, Granada, 18006, Andalusia, Spain*
[c] *Technical University of Catalonia, C. de Jordi Girona 31, Barcelona, 08034, Catalonia, Spain*

Abstract

The present numerical study builds on Ekman (1905)'s work in surface boundary layer and extends the boundary value problem to overcome some of its limitations. Previous studies addressed model's limitations by assuming that deviations from observations are usually ascribed to different eddy viscosity shapes, but seldom to the presence of baroclinic pressure gradients and shallow seas, which are the mainstays of this work. Improved solutions in the ocean boundary layer are obtained considering both depth-dependent wind-induced eddy viscosity and horizontal density gradients, ranging from well-mixed to highly-stratified conditions in a finite-depth ocean. High-order numerical solutions extend those in previous analytical and numerical works in the literature and widens the parameter space analyzed. Remarkably, the current profiles are obtained without ambiguity as a truly superposition of a geostrophic and a ageostrophic terms. Results indicate that, for a vertically-uniform eddy viscosity without density gradients and in shallow waters, currents are practically aligned with wind. As depth increases, misalignment between currents and wind increases and the complexity of the vertical structure increases. At large depths, Ekman's values are attained, i.e., deflection

*Corresponding author
Email addresses: vjllorente@unizar.es (Víctor J. Llorente), vjllorente@ugr.es (Víctor J. Llorente), enrique.padilla@upc.edu (Enrique M. Padilla), mdiezm@ugr.es (Manuel Díez-Minguito)

angles relative to wind direction, θ_W, are $\theta_S - \theta_W = -45°$ at the surface, where the current is maximum, and $\theta_T - \theta_W = -90°$ for the depth-integrated transport (negative for deflections to the right in the Northern Hemisphere). These features remain regardless of the magnitude of the eddy-viscosity. For non-uniform eddy viscosity, $\theta_S - \theta_W$ decreases from $-45°$ up to $-90°$ from low to high stratification level, respectively, whereas $\theta_T - \theta_W$ is rather insensitive ($\theta_T - \theta_W \approx -90°$). Contrary to wind effects, the presence of the only vertically-uniform density gradient forcing, with constant eddy viscosity, deflects the surface angle $\theta_S - \theta_D = +45°$ relative to the density-gradient direction, θ_D, in deep waters. Maximum currents no longer occur at the surface in this case. For non-uniform density-gradient profiles, current magnitude decreases overall while $\theta_S - \theta_D \approx +45°$ as long as the gradient affects the entire surface boundary layer. The deflection angle $\theta_T - \theta_D \sim +95°$ remains less sensitive to changes in density-gradient profile.

Keywords: Wind-driven currents, Baroclinicity-driven currents, Eddy viscosity, Ekman's model, Shallow seas, High-order compact finite difference

---

Índice

1. Introduction

The work of Ekman (1905) on wind-driven currents in the surface boundary layer is a building block of oceanography and helps to explain, for example, upwelling and downwelling phenomena, which are known to have an impact on global circulation and biological productivity. Ekman deduced that the momentum balance for steady horizontal currents in the water column must be between the Coriolis force and the vertical divergence of turbulent shear induced by the wind, namely

$$-fv = K_0 \frac{\partial^2 u}{\partial z^2}\,, \tag{1a}$$

$$fu = K_0 \frac{\partial^2 v}{\partial z^2}\,, \tag{1b}$$

where $u = u(x, y, z)$ and $v = v(x, y, z)$ are the horizontal velocity components along the axes x and y, respectively. Here, K_0 is the vertical eddy viscosity

and f is the inertial frequency (i.e., the Coriolis parameter, which depends on latitude), both constants. The vertical coordinate z is assumed here to be positive upwards and its reference $z = 0$ is set at the surface.

Steady Ekman-derived currents are forced by a uniform wind on the sea surface, i.e., a uniform shear stress in the air-sea interface (τ_w), over an infinite homogeneous water column of constant vertical eddy viscosity K_0. The solution for the vertical profile of the horizontal currents reads

$$u(z) = U_0 \exp\left(\frac{z}{d}\right) \cos\left(\frac{f}{|f|}\left[\frac{z}{d} - \varphi\right]\right) , \tag{2a}$$

$$v(z) = U_0 \exp\left(\frac{z}{d}\right) \sin\left(\frac{f}{|f|}\left[\frac{z}{d} - \varphi\right]\right) , \tag{2b}$$

with $U_0 \coloneqq \sqrt{2}\,\tau_w/(\rho_{\mathrm{ref}}|f|d)$ being a reference velocity at the surface, $d \coloneqq \sqrt{2K_0/|f|}$ the thickness of the surface boundary Ekman layer or depth of friction, $\tau_w = ({\tau_w^x}^2 + {\tau_w^y}^2)^{1/2}$ the wind stress, and $\varphi = \pi/4 - \arctan\left(f/|f|\tau_w^y/\tau_w^x\right)$ is the wind angle (e.g. Price et al., 1987). The solution given by Equations (2) means that the vertical profile of the horizontal currents feature its maximum current at the surface, which is deflected 45° to the right (left) from the wind direction in the Northern (Southern) Hemisphere. Furthermore, the resultant depth-integrated transport is deflected 90° to the right (left) from the wind direction.

Ekman's model cannot be expected to closely match actual observations of wind-driven circulation. It has long been recognized that wind-induced turbulent mixing is expected to be higher in the upper layers. Higher values of the eddy coefficient are expected within layers of uniform density and comparatively small within the transition layers and below mixed layers, thereby being K_0 not constant. Moreover, observations in finite depth seas are influenced not only by wind or bottom boundary layer turbulence but also by baroclinic pressure gradients, which may be crucial in coastal seas influenced by river plumes of local temperature gradients.. The effects of the baroclinic pressure gradients are often disregarded and deviations of observations from Ekman's behavior are usually solely ascribed to depth-dependent shapes of eddy viscosity, but seldom to the presence of baroclinic pressure gradients.

The aim of this study is to evaluate outstanding surface boundary layer features driven both by wind and baroclinic pressure gradients in a non-homogeneous ocean of finite depth. In particular, key features as the deflection angle at the surface, the direction of the depth-integrated net transport,

and the location of the maximum current magnitude in the water column are examined and discussed. The model proposed in this work is in fact an extension of Ekman's. The model considers the balance between the effects of depth-dependent baroclinic pressure gradient, depth-dependent vertical turbulent diffusion and Coriolis. Besides wind shear stress, a horizontal baroclinic pressure gradient is prescribed in the model. Both density and eddy viscosity are separatelly prescribed and allowed to vary with depth according to parameterizations inspired on actual observations. Flexible formulations for eddy viscosity and density field are chosen, thus obtaining a family of shapes capable of mimicking a variety of scenarios, ranging from high to low degrees of stratification, and mixed layer depths. The momentum balance equations of the model are solved numerically with a high-order compact finite-difference method. This method allows accurate solutions to be obtained for current profiles and reduces numerical errors due to discretization. A systhematic sensitivity study of the current profile to changes in eddy viscosity, density gradient, and depth is performed.

The study is organized as follows. Section 2 reviews the literature background regarding extensions of Ekman's model on ocean, and on a lesser extent atmospheric, boundary layer features. Section 3 introduces the equations of the idealized model, including assumptions and simplifications applied, and the depth-dependent parametrizations of eddy viscosity and baroclinic pressure gradient profiles. This Section also presents the decomposition used to characterize the effects of the baroclinic pressure gradient in the Ekman boundary layer, the discretization method, and the design of the experiments. Section 4 contains the validation of the numerical scheme, and the analysis and discussion of the model results regarding its sensibility to changes in eddy viscosity, baroclinic pressure gradient, and depth. The final Section 5 contains the main conclusions of this study. Complementary details concerning the numerical schemes, the convergence analysis, and the limitations of numerical performances are presented in Apéndice˜A.

2. Background

The search for improvements for Ekman's model is still ongoing and often revisited, and a remarkable number of relevant works focusing on different of its features have been published in the past few years.

2.1. Studies on Effects of Depth-dependent Eddy Viscosity

Regarding the issue of the effect of depth-dependent eddy viscosity profiles on wind-driven ocean currents, this has been explored since long in simple set-ups by a considerable number of authors (Rossby, 1932; Dobroklonskiy, 1969; Lai and Rao, 1976; Witten and Thomas, 1976; Madsen, 1977). Lenn and Chereskin (2009) assumed a parameterization of the turbulent stress proportional to the vertical shear of horizontal currents. These authors, building upon the previous work of Chereskin (1995), observed that the currents decay more rapidly than its own veering with depth, thereby resulting in a compression of the time-averaged Ekman spiral that cannot be explained by the classical Ekman theory. Basdurak et al. (2021) showed that the eddy viscosity profile due to wind forcing becomes non-parabolic with increasing stratification. Stratification effects in a bottom Ekman layer, which is related with the depth-varying eddy viscosity profile, have been studied by Cushman-Roisin and Malačič (1997); Taylor and Sarkar (2008); Rosas-Villegas et al. (2020, 2023). Recently, Ezer (2023) evaluated the limitations of the Ekman theory using a realistic physical-based turbulent model that includes shear production turbulence and mixing due to breaking waves.

The parametrization of vertical mixing processes has often been an issue, and still questions arise because particular shapes of the viscosity profiles do not always match realistic conditions. Bressan and Constantin (2019) obtained analytical solutions for weakly perturbed constant viscosity profiles. Dritschel et al. (2020) obtained analytical solutions for piecewise-uniform viscosity, which could mimic a real situation in the ocean when the water column is highly stratified and divided into two layers. Constantin (2021) and Roberti (2021, 2022) further develop the results of Bressan and Constantin (2019), where analytical estimates of the surface deflection angle are derived for different mixing conditions. Both ocean and atmospheric boundary-layer models in non-Cartesian coordinates in a rotating Earth have been explored. Constantin and Johnson (2019) obtained ocean Ekman-type solutions in spherical coordinates using constant eddy viscosity coefficients and Yang et al. (2022, 2023) obtained solutions in ellipsoidal coordinates in the atmospheric boundary layer using altittude-dependent power-law eddy viscosity profiles. Explicit analytical atmospheric Ekman-type solutions with height-dependent eddy viscosities can be extrapolated to the ocean boundary layer (Ionescu-Kruse, 2021; Lyons, 2021; Guan et al., 2022). The study of time-dependent, namely oscillatory, solutions in the ocean was addressed by Craig (1989). Shrira and Almelah (2020) recently studied Ekman wind-driven currents with

eddy viscosity that depend both on time and depth.

2.2. Studies on Effects of Bottom Boundary Layer

Several studies aimed to provide coherent frameworks for the analysis of observations influenced by finite depths, such as those by (e.g.) Winant et al. (2014). Some authors have tried to tackle the issue analytically. Welander (1957); Thomas (1975) studied transient and steady-state wind-driven currents, respectively, at finite depths ($H < \infty$). Thomas (1975) considered an eddy viscosity that varies linearly with depth, from a maximum at the surface to zero at the bottom, which is representative of an unstratified water column. The angular displacement of the surface current from the wind direction is practically zero at very low depths, whereas the displacement tends to $-45°$ when H tends to infinity, as expected from the classical Ekman theory. However, before reaching this limit value of $-45°$, a local maximum of $59°$ is observed. This seems to be consistent with Cushman-Roisin and Deleersnijder (2019). These authors studied shallow-water flows where the upper and lower Ekman layers are coupled. As a result of this coupling, they came up with two dimensionaless functions (F and G) that provide, respectively, the dependence of the geostrophic vorticity on the wind-stress curl and on the wind-stress divergence. These functions F and G undergo overshoots that explain previous observations of local maxima in the deflection angles of the surface current and depth-integrated transport. Furthermore, Cushman-Roisin and Deleersnijder (2019) showed that in shallow seas the top and bottom layers are coupled and not fully developed and, therefore, the depth-integrated transport defection angle is less than the $90°$ relative to the angle of the surface stress.

2.3. Studies on Effects of Depth-dependent Pressure Gradients

The effects of depth-dependent pressure gradients on transport have been largely unexplored. Lentz (1995) studied the sensitivity of inner-shelf circulation to the form of vertical mixing using a steady, linear, unstratified model. The author found that for both along-shelf wind stress and pressure gradient forcing, the along-shelf circulation, unlike the cross-shelf circulation, is insensitive to the form of the eddy viscosity profile. Chu (2015) studied the effect of horizontal density gradients on vertical geostrophic shear, which contributes to current shear that also affects the currents spiral. The hodograph is no longer the classical Ekman spiral because of the presence of a baroclinic pressure gradient. The baroclinic components of the spiral caused by the

horizontally-inhomogeneous density were obtained analytically with the eddy viscosity varying with wind magnitude and depth. The effects were evaluated using monthly climatological mean data on surface wind stress, buoyancy flux, ocean temperature and salinity, and mixed layer depth. However, to fully elucidate the role of baroclinic pressure gradients on the wind-driven flow is still open.

3. Material and Methods

3.1. Basic Equations

The model proposed in this study is an extension of Ekman's. The model considers a steady-state Boussinesq flow with a small Rossby number, i.e. inertia is neglected. Geophysical flow in hydrostatic balance is considered, in which the baroclinic pressure gradient is balanced by rotation and vertical turbulent diffusion. Barometric and barotropic pressure gradients are not considered in the flow. The linear governing equations read as follows

$$-fv = -\frac{g}{\rho_{\mathrm{ref}}}\int_z^0 \frac{\partial \rho}{\partial x}\,\mathrm{d}z + \frac{\partial}{\partial z}\left(K\frac{\partial u}{\partial z}\right), \tag{3a}$$

$$fu = -\frac{g}{\rho_{\mathrm{ref}}}\int_z^0 \frac{\partial \rho}{\partial y}\,\mathrm{d}z + \frac{\partial}{\partial z}\left(K\frac{\partial v}{\partial z}\right). \tag{3b}$$

which are also known as turbulent thermal wind balance (Cronin and Kessler, 2009; Gula et al., 2014; McWilliams and Restrepo, 1999) when first vertically differentiated and then multiplied by the eddy viscosity K. Vertical turbulent diffusion is parameterized by an eddy viscosity profile $K = K(z) > 0$, which is assumed to depend only on the vertical coordinate z. Density ρ is prescribed and allowed to vary both vertically and horizontally, whereas ρ_{ref} is a constant reference density. The rigid-lid approximation is considered. The inertial frequency or Coriolis factor $f = 2\Omega \sin\theta_{\mathrm{lat}}$ is assumed to be constant, with $\Omega = 2\pi/23{,}9345\,\mathrm{rad\,h^{-1}}$ and θ_{lat} being the latitude. The x-axis is aligned with the East-West orientation, pointing East; the y-axis is aligned with the North-South orientation, pointing North.

To close the problem for the velocity field (u, v) in this study, four boundary conditions are imposed: two at the surface ($z = 0$), where a wind-induced stress is assumed, and two at the bed ($z = -H$). These read, res-

pectively,

$$\rho_{\text{ref}}\, K(z=0)\, \frac{\partial u}{\partial z}\bigg|_{z=0} = \tau_w^x\,, \tag{4a}$$

$$\rho_{\text{ref}}\, K(z=0)\, \frac{\partial v}{\partial z}\bigg|_{z=0} = \tau_w^y\,, \tag{4b}$$

and

$$u(z=-H) = u_\star\,, \tag{5a}$$

$$v(z=-H) = v_\star\,, \tag{5b}$$

where $\tau_w^x = \rho_a C_D w_x (w_x^2 + w_y^2)^{1/2}$ and $\tau_w^y = \rho_a C_D w_y (w_x^2 + w_y^2)^{1/2}$ are the two components of surface wind stress with w_x and w_y their respective wind velocities, ρ_a air density, and C_D air-on-water drag coefficient as defined in Wu (1982). The bottom shear velocity components are $u_\star$ and $v_\star$, which are set to 0 under no-slip conditions.

3.2. Homogeneous and Inhomogeneous Descomposition

To evaluate and quantify the influence of baroclinicity in the ocean currents, these can be decomposed into homogeneous and inhomogeneous parts as, respectively,

$$u = u^h + u^i\,, \tag{6a}$$

$$v = v^h + v^i\,, \tag{6b}$$

where (u^h, v^h) are the solutions of the homogeneous linear differential equation, whereas the inhomogenous solution is (u^i, v^i). For convenience, the Boundary Value Problem (BVP) for each part reads, respectively,

$$\begin{cases} -fv^h = \dfrac{\partial}{\partial z}\left(K\dfrac{\partial u^h}{\partial z}\right), \;\; fu^h = \dfrac{\partial}{\partial z}\left(K\dfrac{\partial v^h}{\partial z}\right), & z \in (0,-H) \\ \rho_{\text{ref}} K_0 \left.\dfrac{\partial u^h}{\partial z}\right|_0 = \tau_w^x, \;\; \rho_{\text{ref}} K_0 \left.\dfrac{\partial v^h}{\partial z}\right|_0 = \tau_w^y & z = 0 \\ u^h_{-H} = 0, \;\; v^h_{-H} = 0 & z = -H \end{cases} \tag{7a}$$

and

$$\begin{cases} -fv^i = -\dfrac{g}{\rho_{\text{ref}}}\displaystyle\int_z^0 \frac{\partial \rho}{\partial x}\,\mathrm{d}z + \frac{\partial}{\partial z}\left(K\frac{\partial u^i}{\partial z}\right), \;\; fu^i = -\dfrac{g}{\rho_{\text{ref}}}\displaystyle\int_z^0 \frac{\partial \rho}{\partial y}\,\mathrm{d}z + \frac{\partial}{\partial z}\left(K\frac{\partial v^i}{\partial z}\right), & z \in (0, -H) \\ \rho_{\text{ref}} K_0 \left.\dfrac{\partial u^i}{\partial z}\right|_0 = 0, \;\; \rho_{\text{red}} K_0 \left.\dfrac{\partial v^i}{\partial z}\right|_0 = 0 & z = 0 \\ u^i_{-H} = 0, \;\; v^i_{-H} = 0 & z = -H \end{cases} \tag{7b}$$

The BVP (7a) represents the classical Ekman problem, whereas the non-homogeneities corresponding to the source term can be treated separately in the BVP (7b). The solution of the BVP (7b) can be expressed as a convolution of the Green's function of the differential equation times the baroclinic pressure gradient (e.g. Bressan and Constantin, 2019). Physically, (u^h, v^h) is related to the wind-induced spiral, whereas (u^i, v^i) is related to a baroclinic-induced spiral. Therefore, the currents in Equations (6) are the linear combination of both spirals since the model (3)-(5) is a linear BVP. If any non-linearity occurs in the boundary conditions or in the parameters, this decomposition cannot be performed. The descomposition (6) is used by Chkhetiani et al. (2018) to split and understand the contribution of an atmospheric Ekman boundary layer with bouyancy external force. Section 4.4 further discusses the implications of the decomposition in Equation (6) and the relationship between homogeneous and inhomogeneous solutions and geostrophic and ageostrophic currents.

3.3. Parametrization of the K and ρ profiles

3.3.1. Shape of Eddy Viscosity Profile

The eddy viscosity profile $K(z)$ is parameterized aiming to reproduce a family of shapes that capture key aspects of observed (Yoshikawa and Endoh, 2015) and theoretical (Burchard, 2002) profiles. The latter uses an oceanic turbulence model (Mellor and Yamada, 1982) to derive turbulent viscosity profiles. The behavior of the eddy viscosity, which utterly results from energy transfer by wind shear and the competition between mixing and density stratification, is separated into two regions or layers (Chen and de Swart, 2016). The eddy viscosity $K(z)$ is given by

$$K(z) = \begin{cases} K_0\left[1 - 2\,a\,z_m z + a\,z^2\right] & \text{if } z > z_h \\ K_0\, b \left|\dfrac{z}{z_h}\right|^{-n} & \text{if } z \le z_h \end{cases} \tag{8}$$

where $a = (2\,z_h(z_m - z_h)/n - z_h(z_h - 2\,z_m))^{-1}$ and $b = 2\,a\,z_h(z_m - z_h)/n$ are chosen to keep continuity of both $K(z)$ and $\mathrm{d}K/\mathrm{d}z$ at z_h. The parameters K_0, z_m, and z_h are the eddy viscosity at the surface, the depth at which the eddy viscosity has its maximum value, and the depth at which the two layers in Equation (8) are separated, respectively. The parameter $n \in \mathbb{R}_{\geq 0}$ characterizes how fast the eddy viscosity values decay in the deeper layer from its maximum value as water depth increases. Examples of viscosity profiles according to Equation (8) are shown in Figure 1. Two sets of viscosity profiles can be distinguished for a given value of n:

1. The family of profiles when $z_m/z_h \leq (n+2)/(2n+2)$ [positivity condition]: The eddy viscosity increases its value up to a maximum located at z_m and then, it decreases to 0 with the depth. z_m/z_h links with n to preserve $K(z_m) > 0$ and, therefore, a positive eddy viscosity profile. These kinds of profiles mimic a more stratified water column.

2. The family of profiles when $z_m/z_h \geq 1$: The maximum value of the eddy viscosity is always reached at the surface: $K(z) \leq K_0 \ \forall z$. Now z_m controls the curvature of the first layer. As z_m increases, Equation (8) tends asymptotically to

$$K(z) \simeq \begin{cases} K_0 \left[1 - \dfrac{n}{n+1}\dfrac{z}{z_h}\right] & \text{if } z > z_h \\ K_0 \dfrac{1}{n+1}\left|\dfrac{z}{z_h}\right|^{-n} & \text{if } z \leq z_h \end{cases} \tag{9}$$

   with a linear profile in the upper layer. For small values of z_m/z_h the profiles represent a less stratified water column, resulting in a uniform water column when z_m/z_h is large enough.

In the limit, there are two particular cases of Equation (8):

1. When $n = 0$: The classical Ekman profile is recovered, i.e., $K(z) = K_0 = \text{const}$.

2. When $n \to +\infty$: A zero constant profile is shown below z_h. In such a particular case, $\mathrm{d}K/\mathrm{d}z$ is discontinuous at z_h.

It is worth mentioning the special situation when $z_m = 0$ or $z_m = z_h$. One way or another, the maximum is on the surface but the curvatures are different: $\mathrm{d}^2K/\mathrm{d}z^2 < 0$ when $z_m = 0$, and $\mathrm{d}^2K/\mathrm{d}z^2 > 0$ when $z_m = z_h$.

The influence of waves on the K profile is not explicitly considered in the model, such as (e.g.) Jenkins (1987); Ezer (2023) did. However, it is assumed that this is embedded in each particular $K(z)$ profile, where a non-zero eddy viscosity value, K_0, accounts for mixing at the surface. The parametrization of the eddy viscosity profile given by Equation (8) allows to mimic the effects of different degrees of stratification of the water column, and overcome barely realistic features of previous parametrizations in the literature, such as constant values of K (Craig, 1989; Roberti, 2022) or non-zero asymptotic limits of wind-induced turbulence at large depths (Burchard, 2002).

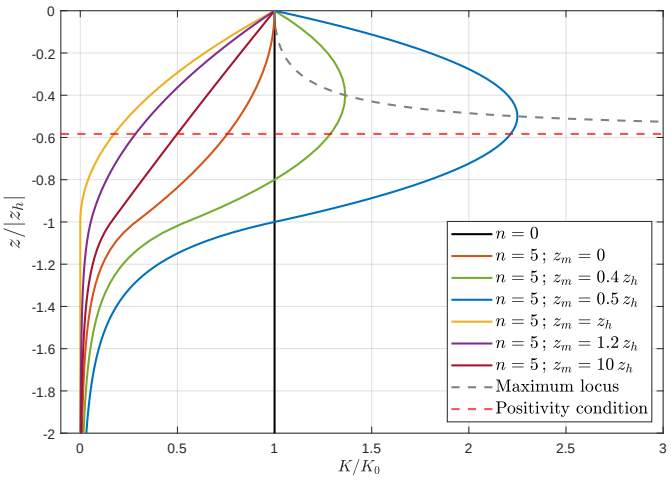

Figura 1: Scaled eddy viscosity profiles from Equation (8). The upper layer (above -1 in the scaled y-axis) combines quadratics laws with $\mathrm{d}^2K/\mathrm{d}z^2 \gtrless 0$ and a linear law with slope $-n/(n+1)$. For all profiles, the lower layer obeys a power decay law that provides $z_m \neq z_h$ and $n \nrightarrow +\infty$.

3.3.2. Shape of the Baroclinic Pressure Gradient

To model the contribution of forces induced by the baroclinic pressure gradient, a density field that is allowed to vary both vertically and horizontally is prescribed. The formulation of the density field presented here aims to be flexible enough to properly mimic realistic conditions given that actual observations of density fields in the ocean show a variety of shapes and scales as long as wide variations of mixing and stratification levels (e.g. Garvine, 1995; Garvine and Monk, 1974; Horner-Devine et al., 2015). This formulation

reads:

$$\rho(s,z) = \frac{\rho(s,0)-\rho(s,-H)}{2}\left[\tanh\left(\frac{z-z_p}{\gamma_v}\right)+1\right]+\rho(s,-H), \tag{10a}$$

$$\rho(s,0) = \frac{\sigma_{\max}}{2}\left[\tanh\left(\frac{1}{\gamma_h}\left(s-\frac{L}{2}\right)\right)+1\right]+\rho_{\mathrm{ref}}, \tag{10b}$$

$$\rho(s,-H) = \frac{\sigma_{\max}}{2}\left[\tanh\left(\frac{1}{\gamma_h}\left(s+\frac{L}{2}\right)\right)+1\right]+\rho_{\mathrm{ref}}, \tag{10c}$$

$$z_p = S_p\, s + z_0, \tag{10d}$$

where z is the vertical coordinate, whereas s is the spatial coordinate aligned with the direction undergoing the largest density gradient (as seen in Figure 2(a)). σ is the potential density regarding a reference density of $\rho_{\mathrm{ref}} = 1000\,\mathrm{kg\,m^{-3}}$ and $\sigma_{\max}$ is the maximum density difference throughout the density field. The degree of horizontal mixing is decoupled from the vertical mixing. These (horinzontal and vertical mixing) are controlled by the parameters γ_h and γ_v, which are, respectively, characteristic horizontal and vertical mixing lengths. The higher γ_h, the higher the horizontal mixing. The higher γ_v, the higher the vertical mixing (lower stratification). The parameter z_p indicates the location of the pycnocline, which changes linearly at a constant rate S_p along the horizontal direction (Equation (10d)). L is the bulk characteristic length of the density front.

Figure 2a shows the tanh-shaped density field modeled by Equation (10) with the parameters indicated in the caption. Vertical and horizontal axes are normalized by the actual water depth (H) and the length of the density front (L), respectively. Panels b-f show five characteristic vertical profiles of the horizontal density gradient at five different locations (marked in panel a). These profiles illustrate that the density field in Equation (10) allows reproducing well-mixed water columns (profiles b and f), two-layer (well-stratified) water columns (profile d) and a range of intermediate situations (profiles c and e). A recent publication by Taylor and Thompson (2023) shows density fronts host numerous instabilities, viz. baroclinic and symmetric instabilities, that can strongly affect turbulence properties.

Two limit cases for the density field arise when $z_p \to +\infty$ and when $z_p \to -\infty$. In both cases, the water column become homogeneous ($\mathrm{d}\rho/\mathrm{d}z = 0$) and the horizontal density gradient becomes independent of the depth ($\mathrm{d}\rho/\mathrm{d}s =$ const). When $z_p \to +\infty$, then Equation (10a) turns into $\rho(s,z) = \rho(s,-H)$. When $z_p \to -\infty$, then Equation (10a) turns into $\rho(s,z) = \rho(s,0)$. Some

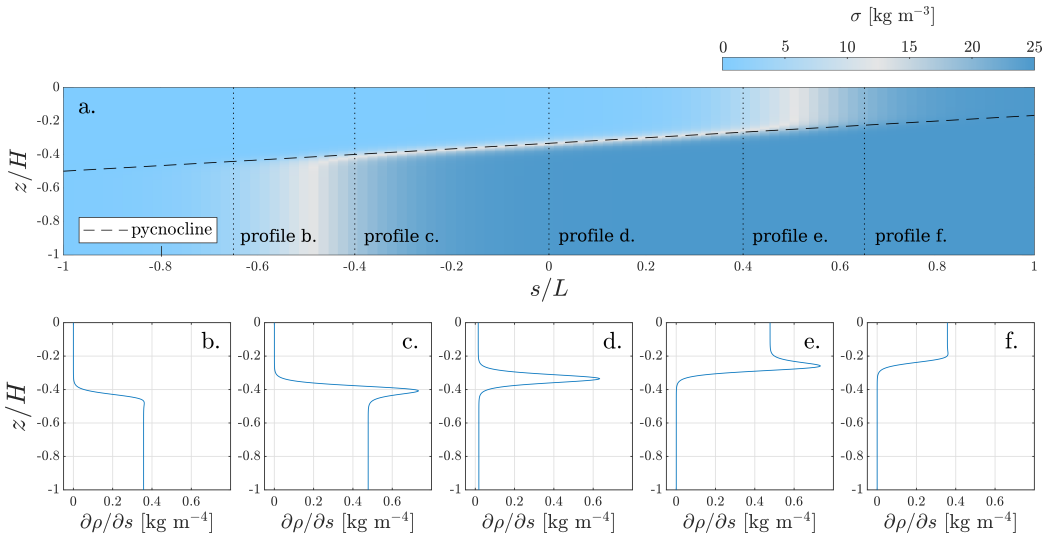

Figura 2: Panel a shows the (potential) density field modeled by Equation (10) with $\sigma_{\max} = 25\,\mathrm{kg\,m^{-3}}$, $\gamma_v = H/30$, $\gamma_h = L/5$, $z_0 = -10\,\mathrm{m}$, $S_p = 0{,}05$, $H = 30\,\mathrm{m}$ and $L = 100\,\mathrm{m}$. The black dashed line indicates the pycnocline. Panels b-f show the horizontal density gradient $\partial\sigma/\partial s$ at five different locations indicated in Panel a (vertical dotted lines).

other particular cases are also reproducible by Equation (10). For instance, the simple triangular shape of the interface between two densities proposed by Lentz and Largier (2006) is achievable for increasing values of S_p.

The advantage of proposing an analytical expression for the density field, such as Equation (10) is that it allows for the analytical expression of the resulting forces induced by baroclinic pressure gradient (term $-g/\rho \int_z^0 \partial\rho/\partial s\,\mathrm{d}z$ in Equation (3)). This analytical expression reads

$$\begin{aligned}\frac{g}{\rho_{\mathrm{ref}}}\int_z^0 \frac{\partial\rho}{\partial s}\mathrm{d}z \;=\; A\Big\{&\gamma_v\left[\tanh^2\mathfrak{s}^+ - \tanh^2\mathfrak{s}^-\right]\left[\ln\left(\frac{\cosh\mathfrak{z}_p}{\cosh\left(\mathfrak{z}-\mathfrak{z}_p\right)}\right) - \mathfrak{z}\right]\\ &+\gamma_h S_p\left[\tanh\mathfrak{s}^- - \tanh\mathfrak{s}^+\right]\left[\tanh\mathfrak{z}_p + \tanh\left(\mathfrak{z}-\mathfrak{z}_p\right)\right]\\ &-2\gamma_v\left[1-\tanh^2\mathfrak{s}^+\right]\mathfrak{z}\Big\}, \end{aligned} \tag{11}$$

where $A = g\sigma_{\max}/(4\rho_{\mathrm{ref}}\gamma_h)$ is a constant and $\mathfrak{s}^\pm = \gamma_h^{-1}[s \pm L/2]$, $\mathfrak{z} = z/\gamma_v$, and $\mathfrak{z}_p = z_p/\gamma_v$ are normalized variables.

3.4. Numerical Solutions

Solutions of the governing Equations (3), with boundary conditions given by Equations (4) and (5), and prescribed eddy viscosity profile and density field parametrized, respectively, by Equation (8) and Equation (10), are obtained numerically. Several Ekman-like analytical solutions with variable parameters were obtained using the WKB method (e.g. Grisogono, 1995; Wenegrat and McPhaden, 2016a; Berger and Grisogono, 1998; Tan, 2001; Wenegrat and McPhaden, 2016b). However, the application of this analytical method depends on the requirement that the characteristics of the medium, such as the eddy viscosity, change more gradually than the solution (Parmhed et al., 2005). This restriction, which could be relevant for certain geophysical flows, justifies the numerical approach in the present study.

The domain is discretized in an equally spaced grid $\Delta z = z_{i+1} - z_i$ in which $z_i = i\Delta z$, $i = 0, 1, \ldots, N-1$, where N is the number of nodes that verifies $-H = (N-1)\,\Delta z$. Consequently, $\phi_i = \phi(z_i)$ for any variable ϕ that depends on the vertical coordinate z.

A high-order finite differentiation based on a Compact Differentiation Scheme (CDS) is considered to solve the momentum balance in Equations (3) (e.g. Lele, 1992). Compact schemes are a class of high-order methods that consider a wide resolution of wavenumbers in the spectral resolution space. The compact stencil allows inner regions to be reached close to the surface and bottom boundaries without further manipulation of the discretization formulae. Compact schemes have been used in a number of environmental applications, (e.g. Chu and Fan, 1999; Kazantsev et al., 2003).

The way to construct a general CDS consists of a linear combination of first derivatives and values at nodes, i.e.

$$\sum_{k\in\mathcal{M}} \alpha_k \left.\frac{\partial\phi}{\partial z}\right|_{i+k} \approx \frac{1}{\Delta z}\sum_{k\in\mathcal{N}} a_k \phi_{i+k}\,. \tag{12}$$

The relations between the coefficients $\{\alpha_k\}$ and $\{a_k\}$ are derived by matching the Taylor series coefficients of $\partial\phi/\partial z|_{i+k}$ and ϕ_{i+k} to the desired order. $\mathcal{M}$ and $\mathcal{N}$ are the stencil sizes. The CDS used in this work is of central type (i.e., $\alpha_0 = 1$ and $\alpha_k = \alpha_{-k}$) and fourth order of accuracy, see details in Apéndice˜A.1.

3.5. Design of Numerical Simulations

A number of sets of numerical simulations (listed in Table 1) are conducted to gain knowledge of key physical features of currents in the ocean

surface boundary layer. These sets include simulations whose solutions are obtained for an ample range of concomitant and realistic, but independent, (i) eddy viscosity profiles and (ii) baroclinic pressure gradients, with changing latitudes, water depths and wind speeds.

Regarding the simulation sets described below, these are the assumptions that are common to all simulations: (i) flat bottom regardless of the water-column depth (H); (ii) density profile changes in the North-South orientation, i.e., $s = y$ in Equation (2), and therefore, $\partial\rho/\partial y \neq 0$; (iii) no-slip conditions at the bottom boundary ($u_\star = v_\star = 0$); and (iv) barotropic pressure gradients being balanced by the geostrophic component of the flow. Note that when a density front effectively exists, the momentum balance is affected and there is a density anomaly (σ) regarding the reference value of density (ρ_{ref}). Therefore, simulations with $\sigma_{\max} = 0$ undergo null baroclinic pressure gradients ($\partial\rho/\partial x = \partial\rho/\partial y = 0$). The density field and the wind speeds are aligned with the North-South axis and pointing as indicated in each simulation set, i.e., $s = y$ (Table 1).

The three sets *P-1*, *P-2*, and *OC* are carried out to validate the numerical model. Sets *P-1* and *P-2* aim to assess the performance of the numerical model. Set *P-1* is inspired by the classical Ekman solution and assumes a vertically-uniform eddy viscosity profile ($n = 0$) for two values of K_0: $0{,}002\,\mathrm{m^2\,s^{-1}}$ and $0{,}02\,\mathrm{m^2\,s^{-1}}$. Set *P-2* is inspired by Dritschel et al. (2020) and assumes a piecewise-constant eddy viscosity profile whose formulation follows Equation (A.12) with $z_h = 0{,}2H$ and two values of l: 0,5 and 2,5. Set *OC*, whose name stands for *Observations by Chereskin (1995)*, aims to reproduce her actual observations. The observations were taken at mid latitudes ($\theta_{\text{lat}} = 37{,}1°$) with an averaged water depth of 4780 m and wind speed components: $w_x = 0{,}43\,\mathrm{m\,s^{-1}}$ and $w_y = -7{,}16\,\mathrm{m\,s^{-1}}$. Results are shown in Section 4.1.

The two sets *KH-1* and *KH-2* aim to analyze the influence of realistic eddy viscosity profiles and finite depths in the BVP (7a). Wind forcing is constant ($10\,\mathrm{m\,s^{-1}}$) and heading North. The resulting profiles of the currents are, thereby, due to changes in K and H, respectively (Table 1). The water column height is varied in the range $1\,\mathrm{m} \leq H \leq 300\,\mathrm{m}$. The shape of the eddy viscosity profile does not change, but the magnitude: $K_0 = 0{,}015\,\mathrm{m^2\,s^{-1}}$ and $K_0 = 0{,}15\,\mathrm{m^2\,s^{-1}}$ for *KH-1* and for *KH-2*, respectively. No baroclinic pressure gradient is considered. Results associated with sets *KH-1* and *KH-2* are presented in Section 4.2.

The sets *BclcLAT-1*, *BclcLAT-2* and *BclcLAT-3* aim to analyze the solely

effects of baroclinic pressure gradients (no wind) in the BVP (7b). These sets undergo density fields whose density gradients induce changing pressure gradients along the y-axis. In *BclcLAT-1*, the density field behaves as an homogeneous water column whose horizontal density gradient is independent of the depth, whereas, in *BclcLAT-2* and *BclcLAT-3* the density field has a very well defined pycnocline 60 m and 140 m below the water surface, respectetively (see Table 1 for further details about the density fields). A mid-latitude ($\theta_{\text{lat}} = 37°$) is considered alongside an Equatorial latitude ($\theta_{\text{lat}} = 0°$); the former provides the context where the Coriolis force is relevant, while the latter provides a limit case of null Coriolis force. In both sets, the eddy viscosity profile is vertically-uniform ($n = 0$) with $K_0 = 0{,}015\,\text{m}^2\,\text{s}^{-1}$, and the water column height is 200 m. Results associated with sets *BclcLAT-1*, *BclcLAT-2* and *BclcLAT-3* are presented in Section 4.3.1.

The sets *BclcHW-1* and *BclcHW-2* aim to analyze the relative contribution of the baroclinic pressure gradients and different wind intensities in the currents for water columns of different height. Therefore, these sets gather simulations with different density fields (responsible for the baroclinic pressure gradients) for a range of depths H and wind intensities W. In *BclcHW-1*, the density field behaves as an homogeneous water column whose horizontal density gradient is independent of the depth, whereas, in *BclcHW-2*, the density field has a very well defined pycnocline 60 m below the water surface (see Table 1 for further detail about the density fields). In both sets, the water column height varies in the range $1\,\text{m} \leq H \leq 200\,\text{m}$, and the wind speed varies in the range $0\,\text{m}\,\text{s}^{-1} \leq |W| \leq 50\,\text{m}\,\text{s}^{-1}$ heading North. Results of *BclcHW-1* and *BclcHW-2* simulations are shown in Section 4.3.2.

Supplementary simulations are carried out to analyze the convergence of the numerical model with the sets *P-1* and *P-2* (see Apéndice˜A.3). Further details about the performance and limitations of the numerical model are in Apéndice˜A.4.

4. Results and Discussion

4.1. Validation of the Numerical Model

To verify the good performance of the high-order scheme, solutions obtained with the CDS were also compared with a standard, low-order finite differentiation scheme (SDS), viz. second order for inner points and first order at the surface (e.g. Chen et al., 2018). Further details of these numerical schemes are given in Apéndice˜A.1 and Apéndice˜A.2.

Cuadro 1: Characterization of the simulation sets. The range of variation of the target variables for each set is highlighted (bold).

Simulation set	$K(z)$ profile	Baroclinic Pressure Grad.	Further environmental variables
P-1	$K_0 \in \{\mathbf{0{,}002}, \mathbf{0{,}02}\}\,\mathrm{m^2\,s^{-1}}$	$\sigma_{\max} = 0\,\mathrm{kg\,m^{-3}}$	$H = 500\,\mathrm{m}$
	$n = 0$		$w_x = 5\,\mathrm{m\,s^{-1}}$
			$w_y = -1\,\mathrm{m\,s^{-1}}$
P-2	Formulation: Eqn. (A.12)	$\sigma_{\max} = 0\,\mathrm{kg\,m^{-3}}$	$H = 900\,\mathrm{m}$
	$l \in \{\mathbf{0{,}5}, \mathbf{2{,}5}\}$		$w_x = 5\,\mathrm{m\,s^{-1}}$
	$z_h = 0{,}2H$		$w_y = 0\,\mathrm{m\,s^{-1}}$
OC	$K_0 = 0{,}0015\,\mathrm{m^2\,s^{-1}}$	$\sigma_{\max} = 0\,\mathrm{kg\,m^{-3}}$	$H = 4780\,\mathrm{m}$
	$n = 1{,}05$		$w_x = 0{,}43\,\mathrm{m\,s^{-1}}$
	$z_m = -18\,\mathrm{m}$		$w_y = -7{,}16\,\mathrm{m\,s^{-1}}$
	$z_h = -25\,\mathrm{m}$		$\theta_{\mathrm{lat}} = 37{,}1^\circ$
KH-1	$K_0 = 0{,}015\,\mathrm{m^2\,s^{-1}}$	$\sigma_{\max} = 0\,\mathrm{kg\,m^{-3}}$	$H = [\mathbf{1}, \mathbf{300}]\,\mathrm{m}$
	$n = [\mathbf{0}, \mathbf{60}]$		$\lvert W\rvert = 10\,\mathrm{m\,s^{-1}}$
	$z_m = -5\,\mathrm{m}$		$\theta_W = 90^\circ$
	$z_h = -10\,\mathrm{m}$		$\theta_{\mathrm{lat}} = 37^\circ$
KH-2	$K_0 = 0{,}15\,\mathrm{m^2\,s^{-1}}$	$\sigma_{\max} = 0\,\mathrm{kg\,m^{-3}}$	$H = [\mathbf{1}, \mathbf{300}]\,\mathrm{m}$
	$n = [\mathbf{0}, \mathbf{60}]$		$\lvert W\rvert = 10\,\mathrm{m\,s^{-1}}$
	$z_m = -5\,\mathrm{m}$		$\theta_W = 90^\circ$
	$z_h = -10\,\mathrm{m}$		$\theta_{\mathrm{lat}} = 37^\circ$
BclcLAT-1	$K_0 = 0{,}015\,\mathrm{m^2\,s^{-1}}$	$\sigma_{\max} = 24\,\mathrm{kg\,m^{-3}}$	$H = 200\,\mathrm{m}$
	$n = 0$	$z_0 \to +\infty$	$\lvert W\rvert = 0\,\mathrm{m\,s^{-1}}$
		$\gamma_h = L/50$	$\theta_{\mathrm{lat}} \in \{\mathbf{0}^\circ, \mathbf{37}^\circ\}$
BclcLAT-2	$K_0 = 0{,}015\,\mathrm{m^2\,s^{-1}}$	$\sigma_{\max} = 24\,\mathrm{kg\,m^{-3}}$	$H = 200\,\mathrm{m}$
	$n = 0$	$z_0 = -60\,\mathrm{m}$	$\lvert W\rvert = 0\,\mathrm{m\,s^{-1}}$
		$\gamma_h = L/50$	$\theta_{\mathrm{lat}} \in \{\mathbf{0}^\circ, \mathbf{37}^\circ\}$
BclcLAT-3	$K_0 = 0{,}015\,\mathrm{m^2\,s^{-1}}$	$\sigma_{\max} = 24\,\mathrm{kg\,m^{-3}}$	$H = 200\,\mathrm{m}$
	$n = 0$	$z_0 = -140\,\mathrm{m}$	$\lvert W\rvert = 0\,\mathrm{m\,s^{-1}}$
		$\gamma_h = L/50$	$\theta_{\mathrm{lat}} \in \{\mathbf{0}^\circ, \mathbf{37}^\circ\}$
BclcHW-1	$K_0 = 0{,}015\,\mathrm{m^2\,s^{-1}}$	$\sigma_{\max} = 24\,\mathrm{kg\,m^{-3}}$	$H = [\mathbf{1}, \mathbf{200}]\,\mathrm{m}$
	$n = 0$	$z_0 \to +\infty$	$\lvert W\rvert = [\mathbf{0}, \mathbf{50}]\,\mathrm{m\,s^{-1}}$
		$\gamma_h = L/50$	$\theta_W = 90^\circ$
			$\theta_{\mathrm{lat}} = 37^\circ$
BclcHW-2	$K_0 = 0{,}015\,\mathrm{m^2\,s^{-1}}$	$\sigma_{\max} = 24\,\mathrm{kg\,m^{-3}}$	$H = [\mathbf{1}, \mathbf{200}]\,\mathrm{m}$
	$n = 0$	$z_0 = -60\,\mathrm{m}$	$\lvert W\rvert = [\mathbf{0}, \mathbf{50}]\,\mathrm{m\,s^{-1}}$
		$\gamma_h = L/50$	$\theta_W = 90^\circ$
			$\theta_{\mathrm{lat}} = 37^\circ$
*Common variables to all sets	Formulation: Equation (8) (except for P-2)	$L = 15 \cdot 10^3\,\mathrm{m}$	$\rho_{\mathrm{ref}} = 1000\,\mathrm{kg\,m^{-3}}$
		$S_p = 0$	$u_\star = v_\star = 0\,\mathrm{m\,s^{-1}}$
		$\gamma_v = H/200$	

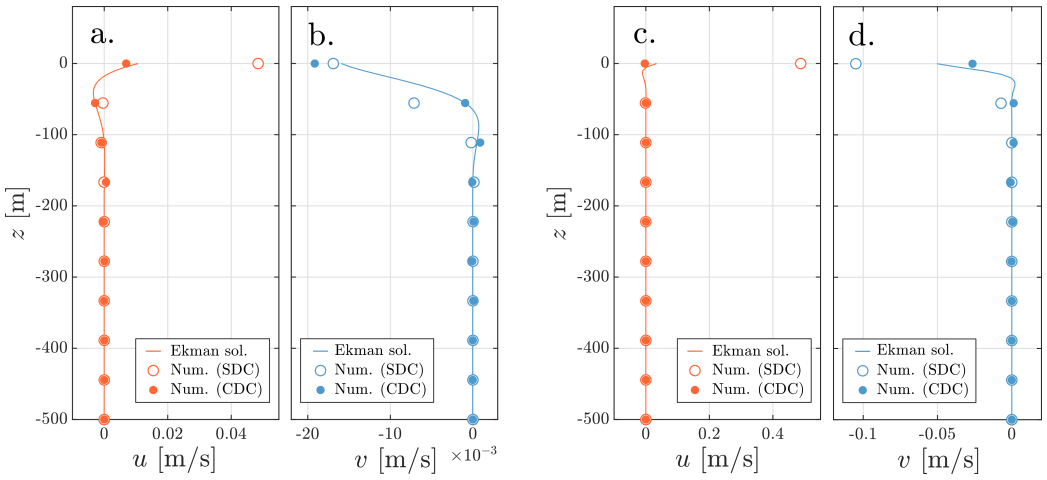

Figura 3: Exact classical Ekman solution (solid lines) compared to numerical solutions following SDC (open circles) and CDC (solid circles) for the current components u (orange) and v (blue). For panels a and b, $K_0 = 0{,}02\,\mathrm{m^2\,s^{-1}}$. For panels c and d, $K_0 = 0{,}002\,\mathrm{m^2\,s^{-1}}$.

Figure 3 illustrates the set *P-1* and shows a comparison between the analytical classical Ekman solution (Equation (2)) and the numerical solutions in which only ten nodes are used, that is, $\Delta z = 55.\overline{5}\,\mathrm{m}$. Such a coarse mesh has been chosen to maximize the differences of the capabilities of both numerical schemes. Panels a and b show that the CDS mimics the analytical Ekman solution far better than the SDS does. This difference is explained by the fact that the CDS undergoes far less numerical diffusion than the SDS. Panels c and d illustrate the particular situation of the Ekman layer thickness being thinner than the discretization mesh. The velocities at surface are far better explained by the CDS than the SCS. The relative error for the x-momentum and y-momentum for SDS are, respectively, twelve and two times larger that the x-momentum and y-momentum for CDS. The source of such large errors is due to the resolution of the mesh.

For the performance case *P-2*, the eddy viscosity shows a discontinuity at z_h (see Equation (A.12)). Figure 4 shows a comparison between analytical (Dritschel et al., 2020) and numerical solutions where only ten nodes are used, i.e., $\Delta z = 100\,\mathrm{m}$. Although CDS loses the order of accuracy (see in Apéndice˜A.3), both components in the velocity field accurately fit the analytical solution. Notice that the boundary condition for v at the surface is $(\partial v/\partial z)_{z=0} = 0$. Since SDS uses a backward scheme at surface, then $v(0) = v(-100)$. Instead, CDS is able to capture the nature of the solution

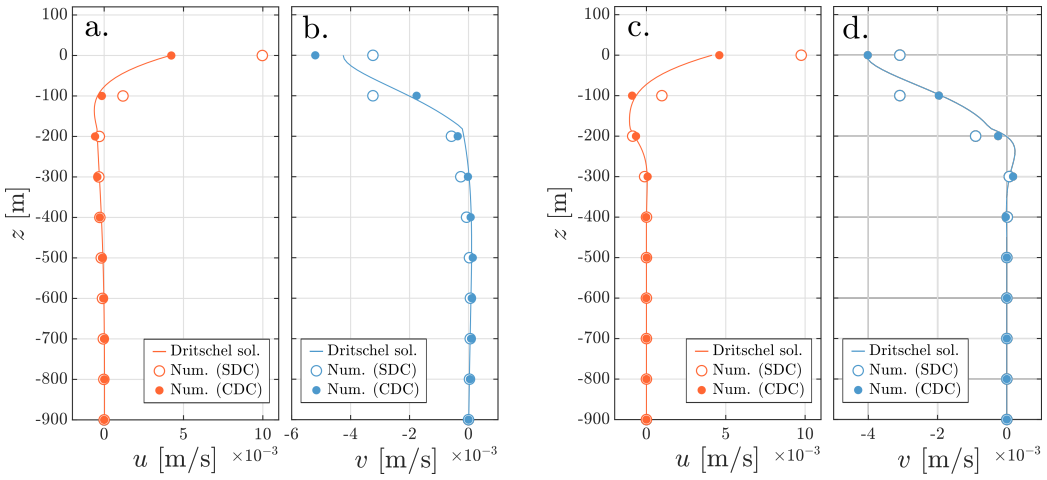

Figura 4: Exact Dritschel solution (solid lines) compared to numerical solutions following SDC (open circles) and CDC (solid circles) for the current components u (orange) and v (blue). For panels a and b, $l = 2{,}5$. For panels c and d, $l = 0{,}5$.

even imposing the derivative to zero.

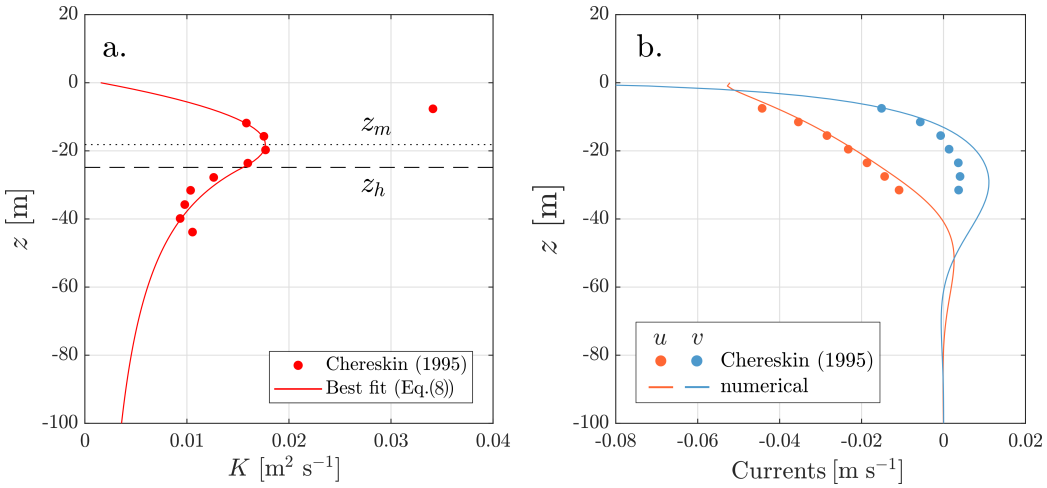

Figura 5: Comparison between observations by Chereskin (1995) and numerical simulations of the set *OC*. Panel a displays the observed eddy viscosity profile (red dots) and the best-fit K profile (red solid line). Panel b displays observed (dots) and numerical current velocities (solid lines) resulting of the best-fit K profile in panel a.

Figure 5 reproduces the results in the Northern Hemisphere by Chereskin (1995) alongside the numerical simulation *OC*. The inferred eddy-viscosity

profile by Chereskin (1995), marked in panel a with red dots, suggests a weak degree of stratification within the upper layer of the ocean. Based on Equation (8), the red curve represents the best-fit K profile, whose parameters are shown in Table 1. Panel b displays the observed (dots) and numerical (solid lines) currents given the particular eddy-viscosity profile displayed in panel a. No pressure gradients are considered. The numerical results are consistent and closely mimic the observations by Chereskin (1995).

4.2. Sensitivity to Changes in Eddy Viscosity Profile and Depth

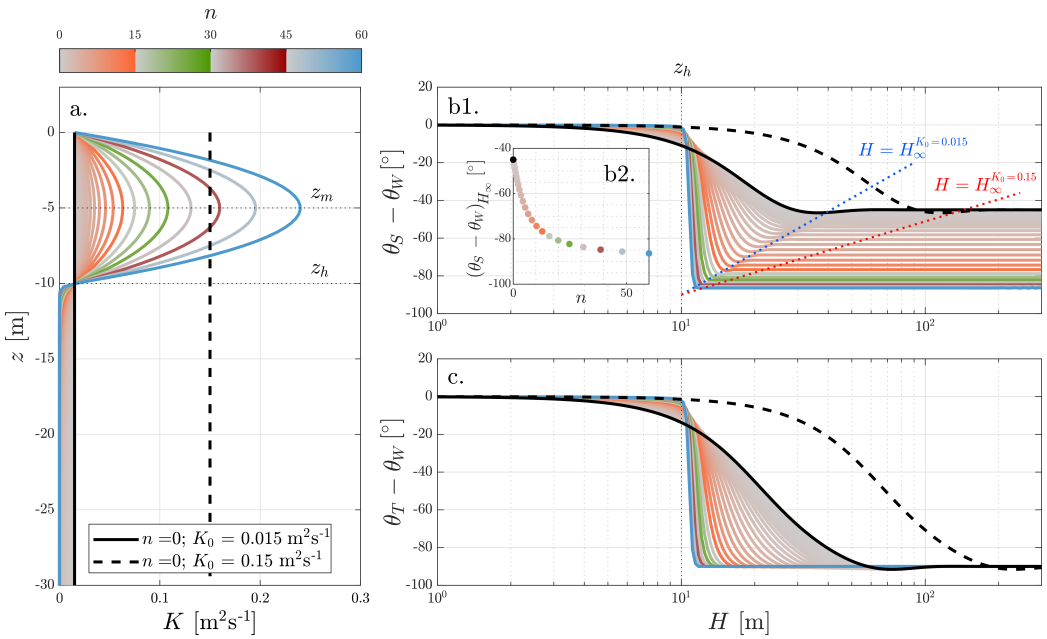

Figura 6: Wind-induced circulation for the eddy viscosity profiles showed in panel a and defined by Equation (8). Panel *b*1 displays the variation of the surface deflection angle $(\theta_S - \theta_W)$ as a function of the water depth, whereas panel *b*2 shows the limit value of $(\theta_S - \theta_W)$ for deep enough water columns (H_∞). Panel *c* displays the depth-integrated mass transport deflection angle $(\theta_T - \theta_W)$. Solid and dashed black lines correspond to the limit cases of a vertically-uniform viscosity profile $(n = 0)$ with $K_0 = 0{,}015\,\mathrm{m^2\,s^{-1}}$ and $K_0 = 0{,}15\,\mathrm{m^2\,s^{-1}}$, respectively. Parameter ranges are those corresponding to cases *KH-1* and *KH-2* (Table 1).

Figure 6 presents the results of the wind-induced circulation in finite-depths given a family of eddy viscosity profiles (these correspond to the sets of simulations *KH-1* and *KH-2* in Table 1). Panel a shows the family of

eddy viscosity profiles considered, where the shape of the profile is preserved. Due to these viscosity profiles and for increasing values of H, panel b1 (and inset b2) illustrates the change of the surface deflection angle of the currents $(\theta_S - \theta_W)$, i.e., the direction of the surface current (θ_S) relative to the direction of the wind (θ_W). Panel c illustrates the sensitivity of the depth-integrated transport deflection angle $(\theta_T - \theta_W)$ to the water column height H.

4.2.1. Surface Deflection Angle

Regarding the surface deflection angle $(\theta_S - \theta_W)$ (panel b1), when the eddy viscosity is constant (i.e., vertically-uniform), there is a gradual change from $(\theta_S - \theta_W) = 0°$ for very shallow water columns to $(\theta_S - \theta_W) = -45°$ for deep enough water columns (H_∞). The latter is the defection angle (to the right from the wind forcing) predicted by the classical Ekman theory. This transition is relatively smooth as the water depth is the only constrain for the rotation of the wind-induced currents. When H is low, wind and currents are aligned $(\theta_S \approx \theta_W)$ as friction is dominant and the water column is not deep enough for the rotation to become relevant in the momentum balance.

For vertically-uniform eddy viscosity profiles ($n = 0$ in panel a), the values $0°$ and $-45°$ are limiting values of $(\theta_S - \theta_W)$ regardless of the value K_0 (see panel b1). However, the transition from $0°$ to $-45°$ occurs at larger depths for $K_0 = 0{,}15\,\mathrm{m^2\,s^{-1}}$ (black dashed curve) than for $K_0 = 0{,}015\,\mathrm{m^2\,s^{-1}}$ (black solid curve). This is due to the fact that the larger the K_0, the larger the surface boundary layer depth. Therefore, Ekman's surface deflection angle $(-45°)$ is only attained when the surface boundary layer depth no longer reaches the bottom.

For non-uniform eddy viscosity profiles ($n \neq 0$ in panel a), Ekman's $-45°$ is no longer the limit value of the surface deflection angle when the water column is deep enough (see panel b1). Instead, the limit value of $(\theta_S - \theta_W)$ grows as n increases: $(\theta_S - \theta_W)$ asymptotically grows from the Ekman's $-45°$ up to $-90°$ for large enough values of n (this growth is seen in inset b2).

The transition of $(\theta_S - \theta_W)$ from $0°$ to its limit value $(\theta_S - \theta_W)_{H_\infty}$ occurs within a range of H, being $\mathcal{O}(10\,\mathrm{m})$ when $n = 0$ and $K_0 = 0{,}015\,\mathrm{m^2\,s^{-1}}$; or $\mathcal{O}(100\,\mathrm{m})$ when $K_0 = 0{,}15\,\mathrm{m^2\,s^{-1}}$. As n increases to larger values, e.g., $n = 60$, the water column effectively separates into two layers (see panel a): an upper layer with high (depth-averaged) values of K, and another lower layer with $K \approx 0\,\mathrm{m^2\,s^{-1}}$. This situation mimics a case of high stratification and explains a far more severe transition of $(\theta_S - \theta_W)$ from $0°$ to $(\theta_S - \theta_W)_{H_\infty}$ within a far shorter range of H $(\mathcal{O}(1\,\mathrm{m}))$ as seen in panel b1. This reduction in

the transitional depth indicates that H_∞ progressively reduces as n increases (blue dotted line in panel b1). The stratification produced by the restriction of the higher values of K to the upper layer when considering large values of n significantly prevents from reaching the boundary-layer depth. In the limit when $n \to \infty$, $H_\infty = z_h$, which effectively means a complete decoupling of the two layers at the water depth z_h.

Thomas (1975) shows hodographs for different values of the ratio H/d and different wind intensities for both a variable and a constant eddy viscosity profile. Thomas (1975) concludes that the resulting hodographs of variable and constant K profile differ considerably in shallow water, which is consistent with the change in the deflection angles observed in Figure 6. To some extent, Figure 6 also suggests that these differences prevail with larger depths. Actually, these differences have already been justified by Welander (1957) given that the consideration of a constant vertical eddy viscosity is, on his view, the most unrealistic assumption of the Ekman model. However, Ezer (2023) noted that even under complex depth-dependent eddy viscosity profiles, in particular cases, the Ekman solution works reasonably well when considering a depth-averaged eddy viscosity value.

Analysing the deflection angle of the surface current, the expected overshoot before reaching its deep-water limit angle exists, as formulated by Cushman-Roisin and Deleersnijder (2019) (similar overshoot exists for the depth-integrated transport). This overshoot is more evident when the eddy viscosity profile is vertically-uniform (black solid line in Figure 6(b1), and located at $H/d \approx 2{,}5$ as illustrated by Cushman-Roisin and Deleersnijder (2019) (see $F(H/d)$ in Fig.1). Similar overshoots had previously been observed (e.g. Thomas, 1975). For very shallow water columns, Thomas (1975) shows that $(\theta_S - \theta_W)$ is, as expected and observed from Figure 6(b1), close to zero. As the water depth increases, so as H/d, $(\theta_S - \theta_W)$ increases reaching a maximum value (overshoot) before reaching its limit value. This overshoot reaches a value of $(\theta_S - \theta_W) = 59°$ according to Thomas (1975), which is larger than the observed overshoot in Figure 6(b1).

4.2.2. Depth-integrated Transport Deflection Angle

The depth-integrated transport is rather insensitive to the particular eddy viscosity profile when H is large enough. As expected, Figure 6c shows that the transport deflection angle $(\theta_T - \theta_W)$ converges into the limit value of Ekman's $-90°$ regardless of the shape of K, in particular, regardless of n. Actually, $(\theta_T - \theta_W)$ remains constant $(-90°)$ for any eddy viscosity profile as

confirmed by Witten and Thomas (1976) for a an exponentially decreasing eddy viscosity profile. It is important to highlight that, in the same conditions, $(\theta_T - \theta_W)$ to reach the limit value of $-90°$ requires, in general, a deeper water column than $(\theta_S - \theta_W)$ to reach its own limit value. The reason for this is that θ_T is an averaged quantity in the entire water column and, therefore, its limit value is only reached when the surface and bottom boundary layers are completely decoupled. This is not the case for θ_S, that requires the two layers to be decoupled only in the surface. It is only when $n \to \infty$ and due to the effect of high stratification levels that the water-column depth necessary for $(\theta_T - \theta_W)$ to reach its limit value equals the depth necessary for $(\theta_S - \theta_W)$ to reach its limit value. This water depth is z_h and, in such circunstances, $(\theta_S - \theta_W) = (\theta_T - \theta_W) = -90°$.

Similarly to the overshoot already observed in Figure 6(b1) for vertically-uniform K profile, $(\theta_T - \theta_W)$ also undergoes an overshoot located at $H/d \approx 4$ as indicated by Cushman-Roisin and Deleersnijder (2019)(see $G(H/d)$ in Fig.1). The same reason above explaining the depth-shift between $(\theta_S - \theta_W)$ and $(\theta_T - \theta_W)$ to reach their limit values applies to the depth-shift of the their overshoots, i.e., $H/d \approx 2{,}5$ for $(\theta_S - \theta_W)$, whereas $H/d \approx 4$ for $(\theta_T - \theta_W)$. Figures 6(b1)-(c) also illustrate that these overshoots in θ_S and θ_T may also exist when the eddy viscosity profile is not uniform (which extends the results by Cushman-Roisin and Deleersnijder (2019)), but becoming much attenuated in stratified water columns.

4.3. Sensitivity to Changes in Density Gradients, Wind and Depth

Inspired by the classical definition of the angles for the surface current and depth-integrated transport relative to the wind forcing direction, similar magnitudes will be pursued in this section relative to the direction of the underlying density-gradient (θ_D). Thus, the surface deflection angle due to a baroclinic pressure gradient is defined as $(\theta_S - \theta_D)$, whereas the depth-integrated transport deflection angle is defined as $(\theta_T - \theta_D)$.

4.3.1. Baroclinic Pressure Gradient Effect in Infinite Depth

The hodographs displayed in Figures 7 and 8 are associated to the simulation sets *BclcLAT-1*, *BclcLAT-2*, and *BclcLAT-3* (Table 1) and show the orientation and magnitude of the currents in the water column when a baroclinic pressure gradient participates in the momentum balance, i.e., when friction and baroclinic pressure gradient forces are balanced by rotation. Uniform K profile and no-wind forcing are considered in *BclcLAT-1*,

BclcLAT-2, and *BclcLAT-3* aiming to analyze solely the role of the baroclinic pressure gradient in the profile of currents (see BVP (7b)). Water depth is large enough ($H > H_\infty$, with H being 200 m), with surface and bottom boundary layers being decoupled.

In the limit case $\theta_{\text{lat}} = 0$ (no-rotation), the Coriolis term is null and the profile of currents in the water column is restricted to the North-South axis (which is the direction of the baroclinic pressure force) and moving opposite to the density gradient. Therefore, both the surface and transport deflection angles are coincident, being $\theta_S = \theta_T = -90°$ (pointing South), or $(\theta_S - \theta_D) = (\theta_T - \theta_D) = 0°$ relative to the density-gradient direction (not showed). The magnitude of the currents grows from a null value at the bottom to a maximum value at the surface. This profile of currents would be different, i.e., a two-layers flow, if imposing mass conservation in the water column rather than null momentum exchange at the air-sea interface. Note that the situation just described (null Coriolis term, baroclinic pressure gradient and mass conservation in the water column) is a typical approximation when describing the estuarine circulation (Hansen and Rattray Jr, 1965). However, all these circulation patterns change when adding the Coriolis contribution. In this case, the maximum current is no longer at the surface (see Figure 7).

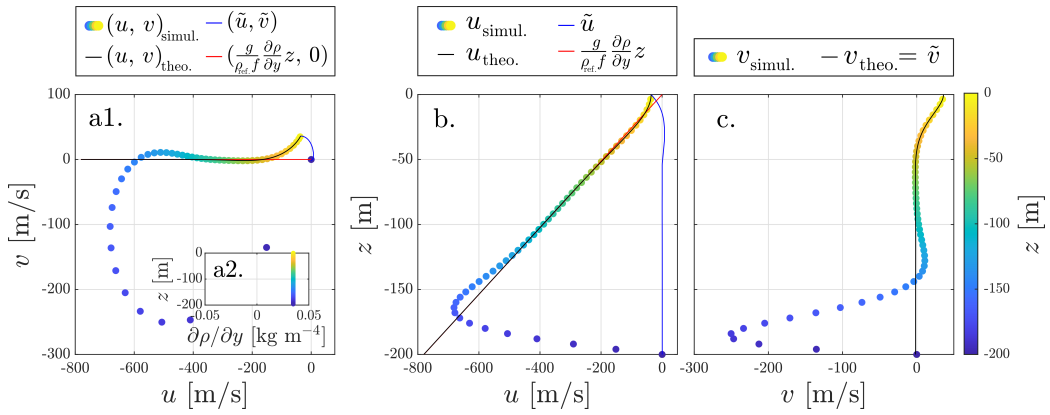

Figura 7: Hodograph and currents belonging to conditions *BclcLAT-1*. Panel a1 displays the hodograph, whereas its inset (a2) displays the undergone density gradient (uniform). Panels b and c display the u, v current components, respectively. The color scheme indicates the depth in the water column.

Figure 7 shows the hodograph (panel a1) and currents (panels b and c) for a typical case with the Coriolis force on ($\theta_{\text{lat}} = 37°$) and uniform density-

gradient profile (inset a2). The addition of the Coriolis contribution alongside a positive uniform density-gradient makes the hodographs to drift towards the West with the current at the surface being deflected $+45°$ to the left from the density-gradient direction. To explain this drift and the surface deflection angle, Figure 7 also includes the analytical solution of the following BVP:

$$\begin{cases} -fv = K_0 \dfrac{\partial^2 u}{\partial z^2}, \;\; fu = \dfrac{g}{\rho_{\text{ref}}} \dfrac{\partial \rho}{\partial y} z + K_0 \dfrac{\partial^2 v}{\partial z^2}, & z \in (0, -H) \\ \rho_{\text{ref}} K_0 \left.\dfrac{\partial u}{\partial z}\right|_0 = 0, \;\; \rho_{\text{ref}} K_0 \left.\dfrac{\partial v}{\partial z}\right|_0 = 0 & z = 0 \\ u_{-H} = -\dfrac{g}{f \rho_{\text{ref}}} \dfrac{\partial \rho}{\partial y} H, \;\; v_{-H} = 0 & z = -H, \end{cases} \tag{13}$$

with $K_0 = 0{,}015\,\mathrm{m^2\,s^{-1}}$ and $\partial\rho/\partial y = 0{,}008\,\mathrm{kg\,m^{-4}}$. Note that imposing the value of $u(z = -H)$ simplifies the problem since no boundary layer develops at the bottom end. Given that the density-gradient and eddy viscosity profiles are constant, the solution currents of he BVP (13) may be linearly decomposed as follows:

$$u = \widetilde{u} + \frac{g}{f \rho_{\text{ref}}} \frac{\partial \rho}{\partial y} z \,, \tag{14a}$$

$$v = \widetilde{v} \,, \tag{14b}$$

with $\widetilde{u}$ and $\widetilde{v}$ being the Ekman-derived steady currents (Equations (2a) and (2b), respectively) forced by a uniform *virtual wind*. This virtual shear stress at the surface is an artifact that, in this case, acts over the x-axis, and whose magnitude depends on the density gradient as $\tau_D^x = -g\, K_0\, f^{-1} (\partial\rho/\partial y)$.

Figure 7-a1 shows that, as expected from Ekman (1905), the hodograph associated to $\widetilde{u}$, $\widetilde{v}$ (blue solid line) develops a clockwise spiral whose surface current is deflected $45°$ to the right from the virtual wind forcing, i.e., $45°$ to the left from the positive density gradient. The current associated to the baroclinic pressure gradient ($g(f\rho_{\text{ref}})^{-1}(\partial\rho/\partial y)z$) is null in the surface and linearly increases with depth heading West (panels a1 and b). Therefore, the total current preserves the $+45°$ deflection angle to the left from the positive density gradient in the surface, and gradually shifts to the West with the depth.

Figure 8 shows the hodographs for typical cases with the Coriolis force on ($\theta_{\text{lat}} = 37°$) and non-uniform density-gradient profiles. These hodographs

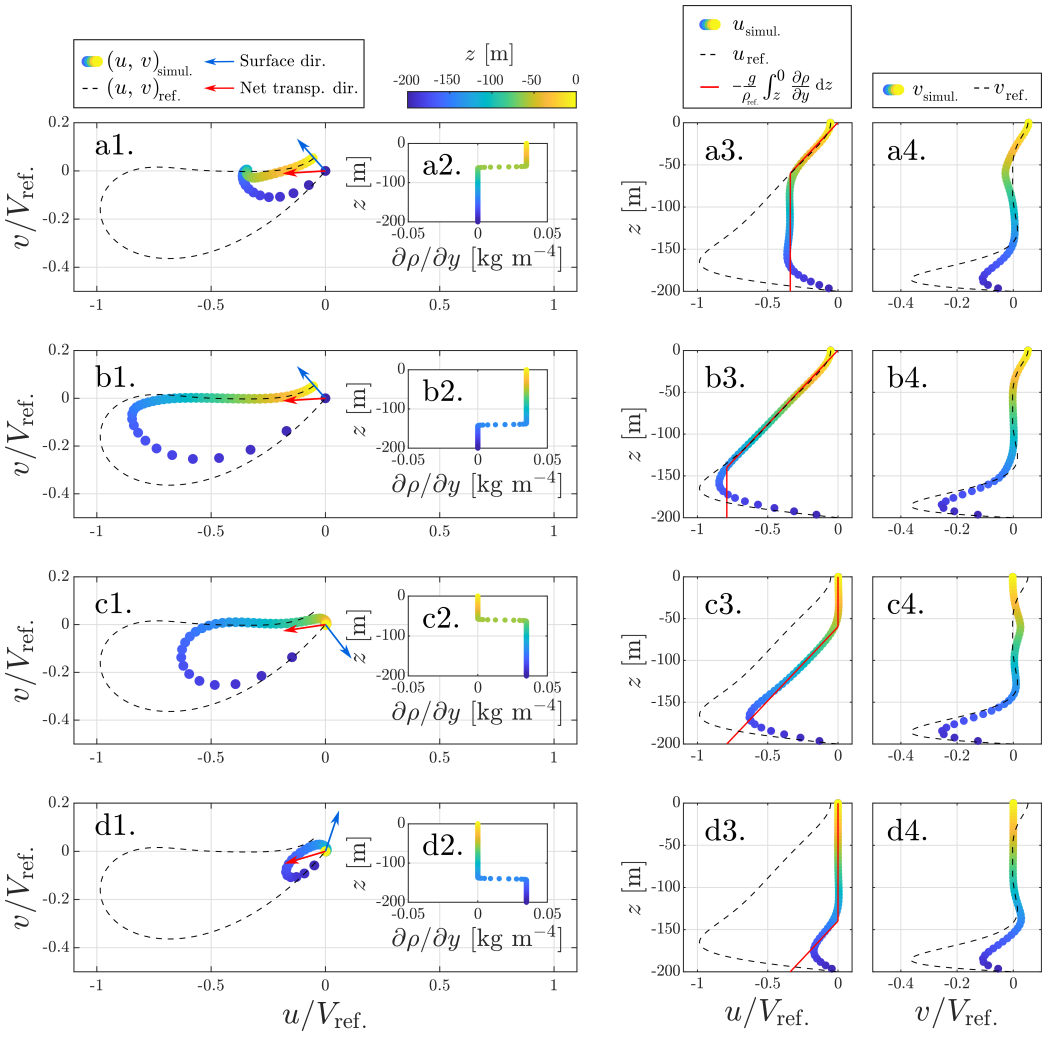

Figura 8: Hodographs and currents belonging to conditions *BclcLAT-1*, *BclcLAT-2*, and *BclcLAT-3*. Panels a1-d1 display the hodographs, whereas their insets display the undergone density gradient (not uniform). Panels a3-d3 and a4-d4 display the u, v current components, respectively. The velocity components are normalized by the maximum current in the reference hodograph (black dashed line in panels a1-d1), i.e., $V_{\text{ref}} = \text{máx}((u_{\text{ref}}^2 + v_{\text{ref}}^2)^{1/2})$. The color scheme indicates the water depth. The directions of the superficial current and depth-averaged mass transport are highlighted with blue and red arrows, respectively.

(panels a1-d1) are respectively derived from the density-gradient profiles illustrated in insets a2-d2. As expected from Figure 7, the Coriolis contribution makes the hodographs to drift towards the West in the northern hemisphere as long as the density gradient heads North. However, the shape of the hodographs, magnitude of the currents, and their surface and transport deflection angles are controlled by the density-gradient profile. The shape of the hodographs is compared to a the reference hodograph (black dashed line), which is the hodograph in Figure 7-a1, derived from the uniform density-gradient profile.

Figure 8, panels a1 and b1, shows the hodographs for the non-uniform density gradients with zero value below the pycnocline (insets a2 and b2). Given the different depth of the pycnocline, the resulting hodographs show changes compared to the reference hodograph: The magnitude of the currents decreases as the density-gradient is undergone by a progressively smaller proportion of the water column; the shape of the hodographs (regardless of the magnitude) changes fundamentally due to a local variation of v at the depth of the pycnocline (see panels a4-d4). These small changes in the hodographs explain small variations in the net transport deflection angle: $+93{,}3°$ (panel a1, red arrow) and $+94{,}4°$ (panel b1, red arrow), which are practically coincident with the transport deflection angle observed in the reference hodograph. At the surface, the direction of the current (blue arrow) is preserved being $+45°$ to the left from the positive density gradient as long as the pycnocline is below the thickness of the surface boundary layer.

Figure 8, panels c1 and d1, shows the hodographs for the non-uniform density gradients with zero value above the pycnocline (insets c2 and d2). As expected, the shape of these hodographs changes compared to the reference one (black dashed line): The magnitude of the currents reduces as the proportion of the water column undergoing the density-gradient decreases; the absence of a density gradient affecting the surface layer makes the surface current to be negligible; and the current associated to the baroclinic pressure gradient ($-g/\rho \int_z^0 \partial\rho/\partial y \, \mathrm{d}z$) progressively grows from the pycnocline downwards (see panels a3-d3).

4.3.2. Baroclinic Pressure Gradient Effects in Finite Depths

Figure 9 displays the changes in hodographs due to baroclinic pressure gradients only (uniform and non-uniform profiles) when the water depth is finite, i.e., there is an overlap between the surface and bottom boundary layers. These hodographs (panels a1-c1) correspond to experiments *BclcHW-*

1 and *BclcHW-2* without wind ($|W| = 0$) and H varying in the range $1\,\text{m} \leq H \leq 200\,\text{m}$ (see color scheme in the legend). Each of these panels has, respectively, an inset (a2-c2) for displaying the shape of the undergone density-gradient profile. Note that the ratio between the depth of the pycnicline and the water depth is fixed and set to 0.3. Panels a3-c3 show the variation of the surface and net transport deflection angles as H increases.

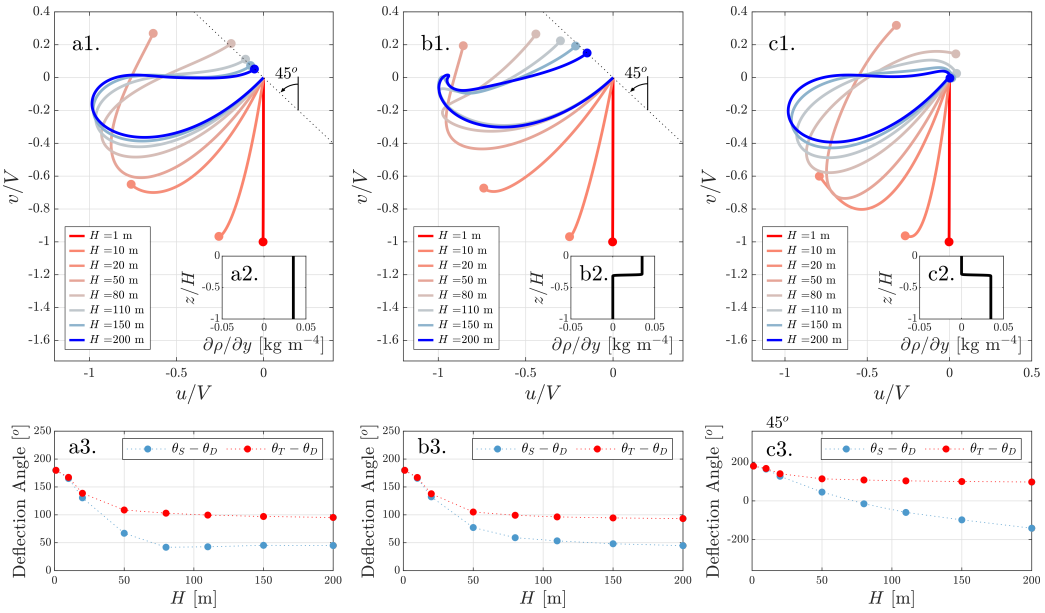

Figura 9: Hodographs belonging to conditions *BclcHW-1* (panel a1) and *BclcHW-2* (panels b1 and c1) where the water-column depth varies in the range $1\,\text{m} \leq H \leq 200\,\text{m}$. For each panel, insets a2, b2 and c2, respectively, display the undergone density gradient. Panels a3, b3 and c3 display the deflection angles of the surface current and the depth-integrated transport. The velocity components are normalized by the maximum current in the water column, i.e., $V = \text{máx}((u^2 + v^2)^{1/2})$.

In the limit, when H is large enough ($H = 200\,\text{m}$), hodographs in Figure 9-a1,b1 (dark-blue solid hodographs) share the following characteristics: the surface and bottom boundary layers are decoupled; the hodographs drift West in the northern hemisphere ($90° \leq (\theta_T - \theta_D) \leq 100°$) due to the combined effect of Coriolis and a heading North density gradient; and $(\theta_T - \theta_D) = +45°$ as long as the density gradient is undergone from the surface. In the other limit, when $H = 1\,\text{m}$ (red solid hodographs in Figure 9), there is a complete overlap of the surface and bottom boundary layers. The currents in the water column are restricted to the North-South axis moving opposite to

the density gradient ($(\theta_S - \theta_D) = (\theta_T - \theta_D) = +180°$) given that the influence of the Coriolis term is overwhelmed by friction in very shallow water depths. Therefore, the magnitude of the currents grows from a null value at the bottom to a maximum value at the surface. Note that an extreme reduction in the water depth results in an analogous situation, in relative terms, to what has already been described above when the Coriolis contribution is null.

In the transition between H being very small to very large, the hodographs in Figure 9 show a progressive drift towards West as the water depth increases. This drift is triggered by the mutual contribution of Coriolis and baroclinic pressure gradients, whose magnitudes become more relevant with larger water depths (note that the currents in Figure 9 are normalized). The differences in the shape of the hodographs are only explained by the differences in the density-gradient profiles, and justifies the different evolutions of $(\theta_S - \theta_D)$ and $(\theta_T - \theta_D)$ observed in panels a3-c3. When the density gradients affects the surface, the transition of $(\theta_S - \theta_D)$ from $+180°$ ($H = 1\,\mathrm{m}$) to $+45°$ ($H = 200\,\mathrm{m}$) is achieved at shallower waters when the density-gradient profile is uniform (panel a3). When the density gradients effects do not affect the surface, $(\theta_S - \theta_D)$ do not converge into any especific direction. In contrast, the transition of $(\theta_T - \theta_D)$ is similar regardless of the density-gradient profile. The small variations in the transition from $+180°$ ($H = 1\,\mathrm{m}$) to around $+95°$ ($H = 200\,\mathrm{m}$) are because θ_T is a depth-integrated quantity in the water column.

4.3.3. Combined Effects of Baroclinic Pressure Gradient, Wind and Depth

Figure 10 focuses in the changes in the surface and net transport deflection angles due to the combined action of baroclinic pressure gradients and wind when the water depth is finite. These results correspond to experiments *BclcHW-1* and *BclcHW-2* with constant wind ($|W| = 10\,\mathrm{m\,s^{-1}}$) and H varying in the range $1\,\mathrm{m} \leq H \leq 200\,\mathrm{m}$ (see color scheme in the legend). Panel a displays the undergone density-gradient field ($0\,\mathrm{kg\,m^{-4}} \leq \partial\rho/\partial y \leq 0{,}035\,\mathrm{kg\,m^{-4}}$), where the pycnicline lives at a fixed ratio $z/H = -0{,}3$. Panels b and c shows the variation of θ_S and θ_T, respectively, relative to the forcing direction θ_0. Note that according to Table 1, the wind and the density gradient are aligned, i.e., the direction of these forcings is coincident in such a way that $\theta_0 = \theta_W = \theta_D$.

Figure 10 must be understood as a spatial assemble of water columns where the currents are resolved for each water column in the y-axis. Therefore, the combination of a constant wind and a baroclinic pressure-gradient

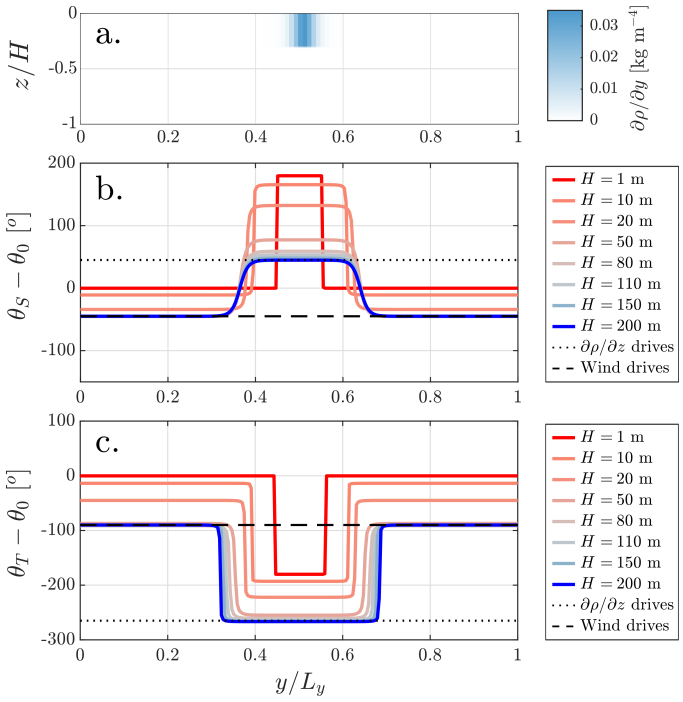

Figura 10: Spatial assemble of water columns whose results correspond to *BclcHW-2*. Panel a displays the vertical distributions of the horizontal density gradient along the North-South axis (y axis). Wind is also acting in the North-South axis. Therefore, density gradient and wind are forcings simultaneously acting in the same direction θ_0. Panels b and c display the deflection angles of the surface current and the depth-integrated transport relative to the forcing direction (θ_0) for different water-column heights (H). The dotted and dashed black lines respectively highlight the expected deflection angles when the currents are mainly driven by the density gradient, or mainly driven by wind.

field means the existance of some water columns where the currents are mainly driven by wind, some others mainly driven by the density gradient, and some others driven by a combination of both. In water columns where $\partial\rho/\partial y$ is negligible (e.g., around $y = 0$ and $y = L_y$), the currents are driven by wind. When H is very low, currents and wind are aligned in the entire column ($(\theta_S - \theta_0) = (\theta_T - \theta_0) = 0^\circ$ in panels b and c). As H increases, the currents progressively turn to the right developing a spiral (not showed) and converging into the classic values of $(\theta_S - \theta_0) = -45^\circ$ and $(\theta_T - \theta_0) = -90^\circ$ when $H = 200\,\mathrm{m}$. In water columns where $\partial\rho/\partial y$ is relevant (e.g., $y = L_y/2$), the currents are driven by the density gradient and the wind forcing is secondary. When H is very low, currents move opposite to the density gradient in the entire water column as already seen in Figures 7-b1 ($(\theta_S - \theta_0) = (\theta_T - \theta_0) = +180^\circ$). As H increases, the currents progressively turns to the left partially explained by a clockwise developing spiral in the surface boundary layer and heading-west currents due to the baroclinic pressure contribution. In the limit ($H = 200\,\mathrm{m}$), $(\theta_S - \theta_0) = +45^\circ$ and $(\theta_T - \theta_0) \approx +95^\circ$ as already seen in Figures 7-b1. There is a particular situation in Figure 10 when surface currents are equaly driven by the wind and by the density gradient. In this situation, $(\theta_S - \theta_0) = 0^\circ$ when $H = 200\,\mathrm{m}$ as a result of the vectorial sum of currents of equal magnitude being deflected $+45^\circ$ to the right of the wind (wind forcing in y-axis) and currents being deflected $+45^\circ$ to the left of the density-gradient (density-gradient forcing in y-axis). For this particular situation, the relationship between the wind and the density-gradient is

$$\left|\frac{\partial\rho}{\partial y}\right| = \frac{f\,\rho_a\,C_D}{g\,K_0} w_y^2, \tag{15}$$

which is derived from the balance between the surface wind stress ($\tau_w = \rho_a\,C_D\,w_y\,|w_y|$) and the virtual wind induced by the density-gradient ($\tau_D = -g\,K_0\,f^{-1}[\partial\rho/\partial y]$). This transition between currents being mainly driven by wind (if $|\partial\rho/\partial y| < f\,\rho_a\,C_D\,w_y^2/(g\,K_0)$), or mainly driven by the density-gradient (if $|\partial\rho/\partial y| > f\,\rho_a\,C_D\,w_y^2/(g\,K_0)$) is explored in Figure 11 for infinite depth ($H = 200\,\mathrm{m}$), and a range of wind intensities ($0\,\mathrm{m\,s^{-1}} \leq |W| \leq 50\,\mathrm{m\,s^{-1}}$) and surface density-gradients ($0\,\mathrm{kg\,m^{-4}} \leq \partial\rho/\partial y \leq 0{,}035\,\mathrm{kg\,m^{-4}}$) still applied over the y-axis.

In Figure 11, the transition between the currents being driven by wind or driven by density-gradient is seen as the jump of $(\theta_S - \theta_0)$ (panel b) from -45° (wind) to $+45^\circ$ (density-gradient) or the jump of $(\theta_T - \theta_0)$ (panel c) from

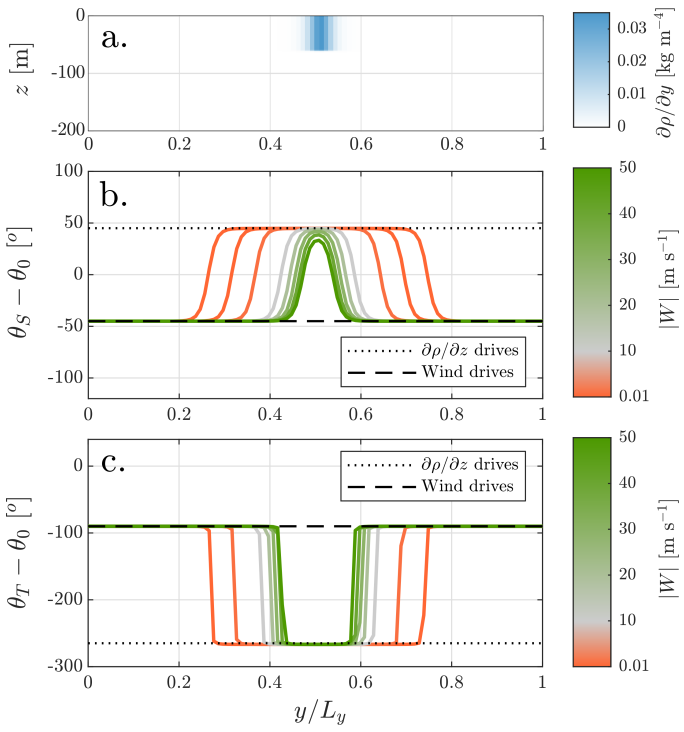

Figura 11: Spatial assemble of water columns whose results correspond to *BclcHW-2*. Panel a displays the vertical distributions of the horizontal density gradient along the North-South axis (y axis). Wind is also acting in the North-South axis. Therefore, density gradient and wind are forcings simultaneously acting in the same direction θ_0. Panels b and c display the deflection angles of the surface current and the depth-integrated transport relative to the forcing direction (θ_0) for different wind speeds ($|W|$). For each line in panels b and c, the color scheme indicates the range of $|W|$, with a color transition at $|W| = 10\,\mathrm{m\,s^{-1}}$. The dotted and dashed black lines respectively highlight the expected deflection angles when the currents are mainly driven by the density gradient, or mainly driven by wind.

$-90°$ (wind) to $\sim +95°$ (density-gradient). The spatial transition between those jumps is controlled by the characteristic horizontal mixing length (γ_h). For a density-gradient field (as given in panel a), the extension of the water columns whose currents are mainly driven by the density gradient shrinks as the wind intensity increases. For example, the density gradient drives the currents from $y/L_y = 0{,}3$ to $y/L_y = 0{,}7$ when $|W| = 0{,}01\,\mathrm{m\,s^{-1}}$, whereas this extension reduces up to four times when the wind escalates to $50\,\mathrm{m\,s^{-1}}$. As seen in Equation (15), the reduction of the area mainly driven by density-gradient as the wind intensifies follows a parabolic law.

4.4. General Considerations on the Reach and Applicability of the Results

4.4.1. On the Geostrophic Balance in the Presence of Baroclinic Pressure Gradients

An important question that may arise when interpreting the results physically, is whether the homogeneous and inhomogeneous part of the solution (7) correspond to geostrophic and ageostrophic currents. Geostrophic balance occurs when the pressure gradient force (usually barotropic) balances the Coriolis force due to rotation. Considering a particular location at the interior of the ocean, far from the influence from surface and bottom boundaries and where the viscous force terms are negligible, Equations (3) reduce to

$$-fv = -\frac{g}{\rho_{\mathrm{ref}}}\int_z^0 \frac{\partial \rho}{\partial x}\,\mathrm{d}z\,, \tag{16a}$$

$$fu = -\frac{g}{\rho_{\mathrm{ref}}}\int_z^0 \frac{\partial \rho}{\partial y}\,\mathrm{d}z\,. \tag{16b}$$

In Equations (16) the (baroclinic) pressure gradient force is balanced by the Coriolis force. Since no barometric nor barotropic contributions are considered in this study, the baroclinic pressure gradient in Equations (16) represents the total pressure gradient. Also, the currents in Equations (16) are still non-divergent, i.e., $\partial u/\partial x + \partial v/\partial y = 0$. Therefore, and given the usual definition of Geostrophic Balance, currents in Equations (16) are geostrophic. Note that currents in Equations (16), which depends on depth, are thus respectively renamed as u^g and v^g. Stewart (2009) refers to them as the relative velocity from the surface at some depth.

If one attempts a decomposition of the Equations (3) in the form $u = u^g + u^a$ and $v = v^g + v^a$, where (u^a, v^a) are the ageostrophic currents, the result is not a decoupling of both currents, but new differential equations

for (u^a, v^a) where the geostrophic term prevails. In other words, the solution cannot be written as the sum of the pressure gradients and the remaining contributions of the motion. Although the general solution (6) is assumed to be a linear superposition of the flow driven by the baroclinic pressure gradient (inhomogeneous solution) and the flow driven by wind (homogeneous solution), it does not imply that the solution corresponds to a linear superposition of a geostrophic flow and an ageostrophic flow. In general, they can not be splitted in separated contributions in the solution. For instance, in Chu (2015), the ageostrophic flow depends on the pressure gradient (see Equation (9) therein). Geostrophic and ageostrophic parts of the flow can not be unambuously separated.

To overcome this issue, in the approach presented in the present study, a more appropriate general decomposition is written in the form $u = \Lambda + u^a$ and $v = \Lambda + v^a$, where $\Lambda = \Lambda(u^g, v^g)$ is a function of geostrophic currents. This approach implies to cancel out the pressure gradients from Equations (3), keeping the value at boundaries for solutions (u^a, v^a). The following asymptotic behaviour should hold:

$$\Lambda \sim (u^g, v^g) \text{ and } (u^a, v^a) \sim 0 \quad \text{far from the boundaries}\,. \tag{17}$$

This generalization provides a context for the decomposition in Equations (6): the inhomogeneous solutions are the geostrophic currents (Λ-function) and the homogeneous solutions are the ageostrophic currents. This decomposition concludes from the differential equations in the BVPs (7) that $(u^i, v^i) \sim (u^g, v^g)$ and $(u^h, v^h) \sim 0$ towards the interior. Consequently, the homogeneous solution of BVP (7a) is a measure and, to some extent, a good indicator of the ageostrophy of the water column.

4.4.2. On the Eddy Viscosity and Density Gradient Relationships

This study considers parameterization formulae to model turbulent viscosity (8) and density (10) that capture key features of both empirical (from observations) and theoretical profiles in the literature. Empirical formulas for parameterization of vertical profiles of eddy viscosity and density gradient are coherently, but separatelly prescibed in the model. Although results are reliable and current profiles resemble observations, it should be recognized that eddy viscosity is not independent of the water column density structure (e.g. high stratification may inhibit the vertical transfer of momentum or density fronts may host instabilities that can strongly affect the eddy profile as described by Taylor and Thompson (2023)). More sofisticated models

may account for this inter-dependence, such as those that compute K based on the Richardson number or more advanced turbulent models (Mellor and Yamada, 1982). Regarding the particular eddy viscosity parametrization, in addition, the influence of wave-induced mixing on the Ekman layer is crudely lumped in a non-zero value of K at the surface. The inclusion of a wave-induced turbulence parametrization in the model could potentially reveal alterations in the upper ocean currents and improve the description of surface temperature (Craig and Banner, 1994; Mellor and Blumberg, 2004; Ezer, 2023). The $K(z)$ profiles considered in the present study exhibit some differences compared to those by Ezer (2023), which uses the 1D turbulent model by Mellor and Yamada (1982). These differences are mainly attributable to surface wave mixing and the influence of density. Although the model presented in this study is more idealized, a complex eddy viscosity profile can be achieved as the linear superposicion of two (or more) different profiles, i.e., $K = K_1 + K_2$ where K_1 and K_2 are convenient profiles from Eqn.(8). The result is a total current $u = u_1 + u_2$, where u_1 and u_2 accounts for the independent contribution of K_1 and K_2 profiles, respectively. This total current may also be interpreted as the contribution of a $K_1 + K_2$ eddy viscosity profile and a residual term which is an artificial baroclinic pressure gradient.

Nevertheless, despite the simplifying assumptions considered in the model, the results presented in this study constitute a step forward in gaining useful insight into wind-induced currents in inhomogeneous water columns of finite depth and, especially, influenced by variable density gradients, which are often neglected.

5. Conclusions and Final Remarks

This study contributes to further understanding the variability of the circulation induced by the combination of viscosity profiles of realistic shape and pressure gradients induced by an idealized density field (which is inspired in buoyant-plumes) in a rotating Earth for a range of finite water depths and wind speeds. Depth-dependent horizontal currents are obtained from the momentum equations as a superposition of baroclinicity- and wind-driven flows, i.e., as a superposition of geostrophic and ageostrophic fully independent flows, respectively. Accurate solutions are computed using a high-order compact scheme differentiation method.

Wind-driven currents in the water column derived from the classical Ekman theory perform a hodograph of well-known characteristics: Deflection

angle between the wind direction and the current at the surface, where the currents are the largest, is 45°; and the angle between the wind direction and the depth-averaged mass transport is 90°. However, these features do not persist under certain conditions where the currents are also forced by finite water depths, by changes in the eddy viscosity profile or by pressure gradients. Therefore, the above characteristics are taken as a reference to study the variability of the circulation given those particular scenarios.

For vertically-uniform eddy viscosity profiles and no density gradients, when H is lower than the mixing depth ($H < z_h$), winds and currents are practically aligned, with $(\theta_S - \theta_W)$ and $(\theta_T - \theta_W)$ in a range of 0° to −10°. When H is large ($H \gg z_h$), wind and currents misalign as described by the classical Ekman theory, i.e., $(\theta_S - \theta_W) = -45°$ and $(\theta_T - \theta_W) = -90°$. These limit values of 0° and −45°, and 0° and −90°, respectively, prevails regardless of the value of K_0. For non-uniform eddy viscosity profiles, the deflection angles grow with the stratification. In particular, the limit value of $(\theta_S - \theta_W)$ grows asymptotically from the Ekman's −45° up to −90° as the stratification increases. In contrast, the limit value of $(\theta_T - \theta_W) = -90°$ is rather insensitive to changes in the stratification. The level of the stratification is also seen to control the range of transition depths between the limiting values for both deflection angles: A more sharp transition is caused by increasing stratification levels.

The baroclinic pressure gradients in the context of Ekman circulation have traditionally received less attention and a systematic study of the variability of the density-gradient induced circulation has not really been addressed in the literature. A relatively versatile formulation is proposed in this paper, aiming to reproduce density fields that mimic realistic density gradients. For a vertically-uniform density gradient, no wind, constant eddy viscosity, mid-latitudes and large depths, the hodograph drift towards the West with the surface current being deflected 45° to the left from the density-gradient direction, i.e., $(\theta_S - \theta_D) = +45°$, or $(\theta_S - \theta_W) = -45°$ if relative to a shear stress at the surface (a *virtual wind*) induced by the density gradient. For non-uniform density-gradient profiles (pycnoclines at different depths), the shape of the hodographs, magnitude of the currents and both surface deflection and transport angles are controlled by the shape of the density-gradient profile. The magnitude of the currents decreases as the density-gradient is undergone by a progressively smaller proportion of the water column. The surface deflection angle is preserved, being 45° to the left from the positive density gradient, as long as the density gradient is undergone in the entire

thickness of the surface boundary layer. The depth-integrated transport angle is, to some extent, far less sentive to the changes in the density-gradient profile as θ_T is a depth-integrated magnitude ($\theta_T - \theta_D \approx +95°$).

When wind and density gradient, acting in the same direction θ_0, compete to drive the currents, the driving forcing is assessed in terms of the variations in $(\theta_S - \theta_0)$ and $(\theta_T - \theta_0)$ from the limit values corresponding to wind-driven currents ($-45°$ and $-90°$, respectively) to the ones corresponding to density-gradient driven currents ($+45°$ and $+95°$, respectively). For the particular situation of both forcings equally driving, the relationship between the density gradient and the wind intensity is analytically proven to be parabolic.

The compact scheme used in this paper for the numerical simulations consists of a linear combination of first derivatives and values at nodes, which could be understood as an extension and enhancement of standard finite differentiation. The inherent complexity of these kind of schemes is compensated by far by the increase in the accuracy and decrease of computational time. Using a compact scheme, the errors in the velocity components decrease significantly, compared to standard differentiation, and they become comparable even in the worst scenario. i.e, resolving the circulation given a piecewise-constant eddy viscosity profile. In terms of computational time, a compact scheme is seen to speed up the solution by more than one order of magnitude compared to its standard counterpart (once the simulations are in the asymptotic region).

Apéndice A. Details of the Numerical Schemes

Apéndice A.1. Compact Finite Difference Scheme (High Order)

In order to compute derivatives based on high-accuracy methods, this paper uses a fourth-order central compact differentiation scheme. The vertical diffusion terms are discretized in a conservative form, applying twice a first-derivative compact scheme. To do so, the Ekman model is split as follows:

$$-fv = T^x + \frac{\partial q^x}{\partial z}\,, \qquad q^x = K\frac{\partial u}{\partial z}\,, \tag{A.1a}$$

$$fu = T^y + \frac{\partial q^y}{\partial z}\,, \qquad q^y = K\frac{\partial v}{\partial z}\,. \tag{A.1b}$$

where $q^x = q^x(z)$ and $q^y = q^y(z)$ are the diffusive flux components along x and y axes. The total pressure gradients in both components are $T^x =$

$-g/\rho_{\text{ref}} \int_z^0 \partial\rho/\partial x \, \mathrm{d}z$ and $T^y = -g/\rho_{\text{ref}} \int_z^0 \partial\rho/\partial y \, \mathrm{d}z$, respectively. A fourth-order numerical scheme of an inner region ($2 \leq i \leq N-3$) is written as

$$\frac{1}{4} \left.\frac{\partial\phi}{\partial z}\right|_{i-1} + \left.\frac{\partial\phi}{\partial z}\right|_{i} + \frac{1}{4} \left.\frac{\partial\phi}{\partial z}\right|_{i+1} \approx \frac{3}{2} \frac{\phi_{i+1} - \phi_{i-1}}{2\Delta z} \,, \tag{A.2}$$

where ϕ represents either q^x, q^y, u or v. For the inner node adjacent to the surface ($i = 1$) and to the bottom ($i = N-2$), the boundary conditions (4)-(5) should be applied in the left-, right-hand side of Equation (A.2) where applicable. On the other hand, only for the discretization of q^x and q^y at the surface ($i = 0$), u and v at the bottom ($i = N-1$) is necessary to write a boundary-closure scheme to mimic the implicit nature and formal order of accuracy of the interior scheme (A.2) but avoid the use of points outside the domain. For example, a fourth-order boundary scheme at the point 0 is written as

$$\left.\frac{\partial\phi}{\partial z}\right|_{0} + 3 \left.\frac{\partial\phi}{\partial z}\right|_{1} \approx \frac{1}{\Delta z} \left(-\frac{17}{6}\phi_0 + \frac{3}{2}\phi_1 + \frac{3}{2}\phi_2 - \frac{1}{6}\phi_3 \right) .$$

being ϕ_0 the boundary condition (4). For a boundary scheme at the point $N-1$, the left-hand side coefficient of the point $N-2$ is the left-hand side coefficient of the point 1 of the above formula. The right-hand side coefficients of the points $N-1$, $N-2$, $N-3$, and $N-4$ are the negative coefficients obtained in the above formula for the points 0, 1, 2, and 3. The value of ϕ_{N-1} corresponds to the boundary condition (5). Substituting derivatives from Equations (A.1a) and (A.1b) into previous formulae and with a bit of algebra, the numerical scheme results in the linear system of equations:

$$\begin{bmatrix} \mathbf{W}_u & \mathbf{D} & \mathbf{0} & \mathbf{0} \\ \mathbf{0} & \mathbf{W}_q & \mathbf{F} & \mathbf{0} \\ \mathbf{0} & \mathbf{0} & \mathbf{W}_u & \mathbf{D} \\ -\mathbf{F} & \mathbf{0} & \mathbf{0} & \mathbf{W}_q \end{bmatrix} \begin{bmatrix} \mathbf{u} \\ \Delta z\, \mathbf{q}^x \\ \mathbf{v} \\ \Delta z\, \mathbf{q}^y \end{bmatrix} = \begin{bmatrix} \mathbf{M}_q & \mathbf{0} & \mathbf{0} & \mathbf{0} \\ \mathbf{0} & \mathbf{M}_q & \mathbf{0} & \mathbf{0} \\ \mathbf{0} & \mathbf{0} & \mathbf{M}_q & \mathbf{0} \\ \mathbf{0} & \mathbf{0} & \mathbf{0} & \mathbf{M}_q \end{bmatrix} \begin{bmatrix} \mathbf{0} \\ \mathbf{b}^x \\ \mathbf{0} \\ \mathbf{b}^y \end{bmatrix} + \begin{bmatrix} \mathbf{b}^x_{1,\text{BC}} \\ \mathbf{b}^x_{2,\text{BC}} \\ \mathbf{b}^y_{1,\text{BC}} \\ \mathbf{b}^y_{2,\text{BC}} \end{bmatrix} , \tag{A.3}$$

where vectors and matrices are defined, respectively, as follows:

$$\mathbf{u} \coloneqq (u_0, u_1, \ldots, u_{N-3}, u_{N-2})^T\,, \tag{A.4a}$$
$$\mathbf{v} \coloneqq (v_0, v_1, \ldots, v_{N-3}, v_{N-2})^T\,, \tag{A.4b}$$
$$\mathbf{q}^x \coloneqq (q_1^x, q_2^x, \ldots, q_{N-2}^x, q_{N-1}^x)^T\,, \tag{A.4c}$$
$$\mathbf{q}^y \coloneqq (q_1^y, q_2^y, \ldots, q_{N-2}^y, q_{N-1}^y)^T\,, \tag{A.4d}$$
$$\mathbf{b}^x \coloneqq -\Delta z^2 (T_0^x, T_1^x, T_2^x, \ldots, T_{N-3}^x, T_{N-2}^x)^T\,, \tag{A.4e}$$
$$\mathbf{b}^y \coloneqq -\Delta z^2 (T_0^y, T_1^y, T_2^y, \ldots, T_{N-3}^y, T_{N-2}^y)^T\,, \tag{A.4f}$$
$$\mathbf{b}^x_{1,\mathrm{BC}} \coloneqq -u_\star \mathbf{w}_u - \Delta z[\tau_w^x/(\rho_{\mathrm{ref}} K_0)]\mathbf{m}_u\,, \tag{A.4g}$$
$$\mathbf{b}^x_{2,\mathrm{BC}} \coloneqq -\Delta z[\tau_w^x/\rho_{\mathrm{ref}}]\mathbf{w}_q + \Delta z^2[T_{N-1}^x + f v_\star]\mathbf{m}_q\,, \tag{A.4h}$$
$$\mathbf{b}^y_{1,\mathrm{BC}} \coloneqq -v_\star \mathbf{w}_u - \Delta z[\tau_w^y/(\rho_{\mathrm{ref}} K_0)]\mathbf{m}_u\,, \tag{A.4i}$$
$$\mathbf{b}^y_{2,\mathrm{BC}} \coloneqq -\Delta z[\tau_w^y/\rho_{\mathrm{ref}}]\mathbf{w}_q + \Delta z^2[T_{N-1}^y - f u_\star]\mathbf{m}_q\,, \tag{A.4j}$$
$$\mathbf{w}_u = (0, 0, \ldots, 3/4, 17/6)^T\,, \tag{A.4k}$$
$$\mathbf{m}_u = -(-1/4, 0, 0, \ldots, 0)^T\,, \tag{A.4l}$$
$$\mathbf{w}_q = (-17/6, -3/4, 0, \ldots, 0)^T\,, \tag{A.4m}$$
$$\mathbf{m}_q = -(0, 0, \ldots, -1/4)^T\,, \tag{A.4n}$$

and

$$\mathbf{F} \coloneqq f\Delta z^2 \mathbf{M}_q, \quad \mathbf{D} \coloneqq -\mathbf{M}_u \mathbf{K}^{-1}, \quad \mathbf{K} \coloneqq \mathrm{diag}(K_1, K_2, \ldots, K_{N-1})\,, \tag{A.5a}$$

$$\mathbf{W}_u = \begin{pmatrix} -3/4 & 0 & 3/4 & & \\ & -3/4 & 0 & 3/4 & \\ & & \ddots & \ddots & \ddots \\ & & & -3/4 & 0 \\ & & 1/6 & -3/2 & -3/2 \end{pmatrix}, \quad \mathbf{M}_u = -\begin{pmatrix} 1 & 1/4 & & & \\ 1/4 & 1 & 1/4 & & \\ & \ddots & \ddots & \ddots & \\ & & 1/4 & 1 & 1/4 \\ & & & 3 & 1 \end{pmatrix} \tag{A.5b}$$

$$\mathbf{W}_q = \begin{pmatrix} 3/2 & 3/2 & -1/6 & & \\ 0 & 3/4 & & & \\ -3/4 & 0 & 3/4 & & \\ & \ddots & \ddots & \ddots & \\ & & -3/4 & 0 & 3/4 \end{pmatrix}, \quad \mathbf{M}_q = -\begin{pmatrix} 1 & 3 & & & \\ 1/4 & 1 & 1/4 & & \\ & \ddots & \ddots & \ddots & \\ & & 1/4 & 1 & 1/4 \\ & & & 1/4 & 1 \end{pmatrix} \tag{A.5c}$$

The minus sign is established in $\mathbf{M}_u$, $\mathbf{M}_q$, $\mathbf{m}_u$, and $\mathbf{m}_q$ due to $z \le 0$, while some components of the block vector, $[\mathbf{u},\, \Delta z\, \mathbf{q}^x,\, \mathbf{v},\, \Delta z\, \mathbf{q}^y]^T$, multiply by Δz so that it has the same dimensions.

Apéndice A.2. Standard Finite Difference Scheme (Low Order)

Using the same notation as in Equation (A.1), a second-order central scheme for $1 \leq i \leq N-2$ is considered for the vertical diffusion term, i.e.,

$$\left.\frac{\partial q^x}{\partial z}\right|_i = \left.\frac{\partial}{\partial z}\left(K\frac{\partial u}{\partial z}\right)\right|_i \approx \frac{K_{i-1/2}u_{i-1} - 2\overline{K}_i u_i + K_{i+1/2}u_{i+1}}{\Delta z^2}\,, \tag{A.6}$$

where $\overline{K}_i := (K_{i-1/2} + K_{i+1/2})/2$, while a backward first-order finite difference scheme for $i = 0$ is considered, i.e.,

$$\left.\frac{\partial u}{\partial z}\right|_0 \approx \frac{u_0 - u_1}{\Delta z}\,, \tag{A.7a}$$

that, after applying the boundary condition (4a), the velocity at the surface is obtained: $u_0 = u_1 + \Delta z\,\tau_w^x/(\rho_{\text{ref}}K_0)$. Equations (A.6 and (A.7a) apply in a similar way to the y component of the diffusive flux and velocity.

After some mathematical manipulations, the numerical scheme results in the following linear system:

$$\begin{bmatrix} \mathbf{D} & \mathbf{F} \\ -\mathbf{F} & \mathbf{D} \end{bmatrix} \begin{bmatrix} \mathbf{u} \\ \mathbf{v} \end{bmatrix} = \begin{bmatrix} \mathbf{I} & \mathbf{0} \\ \mathbf{0} & \mathbf{I} \end{bmatrix} \begin{bmatrix} \mathbf{b}^x \\ \mathbf{b}^y \end{bmatrix} + \begin{bmatrix} \mathbf{b}^x_{\text{BC}} \\ \mathbf{b}^y_{\text{BC}} \end{bmatrix}\,, \tag{A.8}$$

where vectors and matrices are defined, respectively, as follows:

$$\mathbf{u} := (u_1, u_2, \ldots, u_{N-3}, u_{N-2})^T\,, \tag{A.9a}$$
$$\mathbf{v} := (v_1, v_2, \ldots, v_{N-3}, v_{N-2})^T\,, \tag{A.9b}$$
$$\mathbf{b}^x := -\Delta z^2 (T_1^x, T_2^x, \ldots, T_{N-3}^x, T_{N-2}^x)^T\,, \tag{A.9c}$$
$$\mathbf{b}^y := -\Delta z^2 (T_1^y, T_2^y, \ldots, T_{N-3}^y, T_{N-2}^y)^T\,, \tag{A.9d}$$
$$\mathbf{b}^x_{\text{BC}} := (-\Delta z (K_{1/2}/K_0)\tau_w^x/\rho_{\text{ref}}, 0, \ldots, 0, -K_{N-3/2}u_\star)^T\,, \tag{A.9e}$$
$$\mathbf{b}^y_{\text{BC}} := (-\Delta z (K_{1/2}/K_0)\tau_w^y/\rho_{\text{ref}}, 0, \ldots, 0, -K_{N-3/2}v_\star)^T\,, \tag{A.9f}$$

and

$$\mathbf{F} := f\Delta z^2 \mathbf{I}, \quad \mathbf{D} := \begin{pmatrix} -K_{3/2} & K_{3/2} & & & \\ K_{3/2} & -2\overline{K}_2 & K_{5/2} & & \\ & \ddots & \ddots & \ddots & \\ & & K_{N-7/2} & -2\overline{K}_{N-3} & K_{N-5/2} \\ & & & K_{N-5/2} & -2\overline{K}_{N-2} \end{pmatrix}, \tag{A.10}$$

with $\mathbf{I}$ being the $(N-2)\times(N-2)$ identity matrix.

Apéndice A.3. Convergence Analysis

Convergence analysis assesses the accuracy of the target numerical schemes, that are, standard finite differences and compact finite differences. Two numerical performances are thus designed, where the numerical velocities are compared with the analytical solutions given by the classical Ekman theory and the analytical solutions obtained by Dritschel et al. (2020). Aiming to quantify the difference between numerical and analytical results, the l_2-norm of the error is used to monitor the root-mean-square error:

$$||u_{\text{num.}} - u_{\text{ana.}}||_2 = \left(\frac{1}{N} \sum_{i=0}^{N-1} \left(u_i|_{\text{num.}} - u_i|_{\text{ana.}} \right)^2 \right)^{1/2} , \tag{A.11a}$$

and similar for v.

For the performances *P-1* with $K_0 = 0{,}02\,\mathrm{m^2\,s^{-1}}$, the results for the convergence rates are showed in Figure A.12a. The results indicate that the Standard Differenciation Scheme (SDS) behaves as a first-order scheme for $\Delta z < 50\,\mathrm{m}$, whereas the Compact Differenciation Scheme (CDS) behaves as a fourth-order scheme for interval sizes within $[125, 25]\,\mathrm{m}$. The decrease of accuracy in the SDS is because the global error is what is being evaluated in the domain and the scheme is first-order at the boundary. These two facts control the computed errors overall. On the other hand, CDS performs better and similar accuracy for both component of the velocity than the Standard one.

Figure A.12b displays the l_2-norm of the error as a function of the CPU time. Simulations were run using an Intel(R) Core(TM) i7-5500U CPU @ 2.40 GHz. In regions of low accuracy, the CPU time of CDS is slightly larger than the SDS. Once the convergence rate is reached (l_2-norm $< 10^{-4}$), the computational time of SDS largely increases, whereas CPU time for CDS remains around 0,1 seconds.

For the performance *P-1* with $K_0 = 0{,}002\,\mathrm{m^2\,s^{-1}}$, the results for the convergence rates are showed in Figure A.12c. Qualitatively, both numerical schemes display performances that remind to the ones observed in Figure A.12a. However, the residuals are one order of magnitude lower than those for $K_0 = 0{,}02\,\mathrm{m^2\,s^{-1}}$. Just comparing between SDS and CDS, the highest accuracy for SDS (l_2-norm $\approx 10^{-5}$) is achieved when $\Delta z = 0{,}1\,\mathrm{m}$, whereas CDS reaches the same accuracy simply using a far more coarse grid ($\Delta z = 10\,\mathrm{m}$). At $\Delta z = 0{,}1\,\mathrm{m}$, CDS reaches machine accuracy (l_2-norm $\approx 10^{-13}$). On the whole, CDS works better than a SDS.

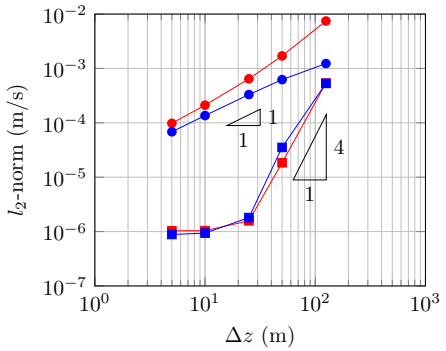

(a) Errors with $K_0 = 0{,}02\,\mathrm{m^2\,s^{-1}}$

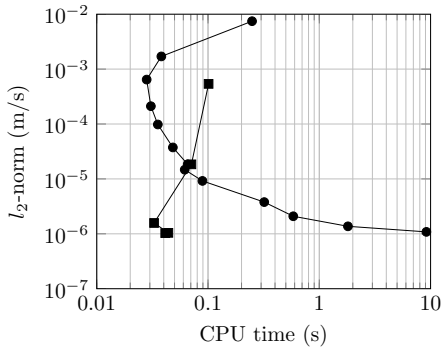

(b) CPU time with $K_0 = 0{,}02\,\mathrm{m^2\,s^{-1}}$

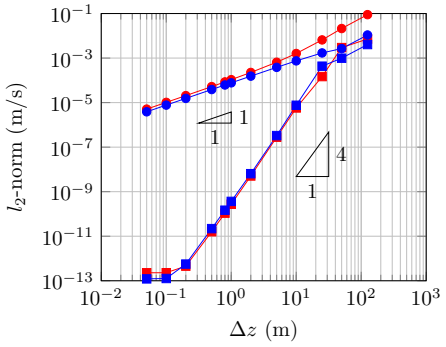

(c) Errors with $K_0 = 0{,}002\,\mathrm{m^2\,s^{-1}}$

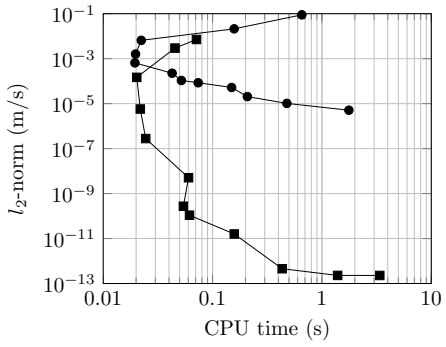

(d) CPU time with $K_0 = 0{,}002\,\mathrm{m^2\,s^{-1}}$

Figura A.12: Convergence plots at left for u (red) and v (blue), using SDS (dots) and CDS (squares). Computational time plots at right for SDS (dots) and CDS (squares).

Figure A.12d displays the l_2-norm versus the CPU time. CDS achieves greater accuracy than SDS after a far shorter CPU time. For instance, for a norm of 10^{-5}, 1 second using CDS becomes 22 seconds using SDS. Likewise, machine accuracy using CDS is achieved in just 1 second.

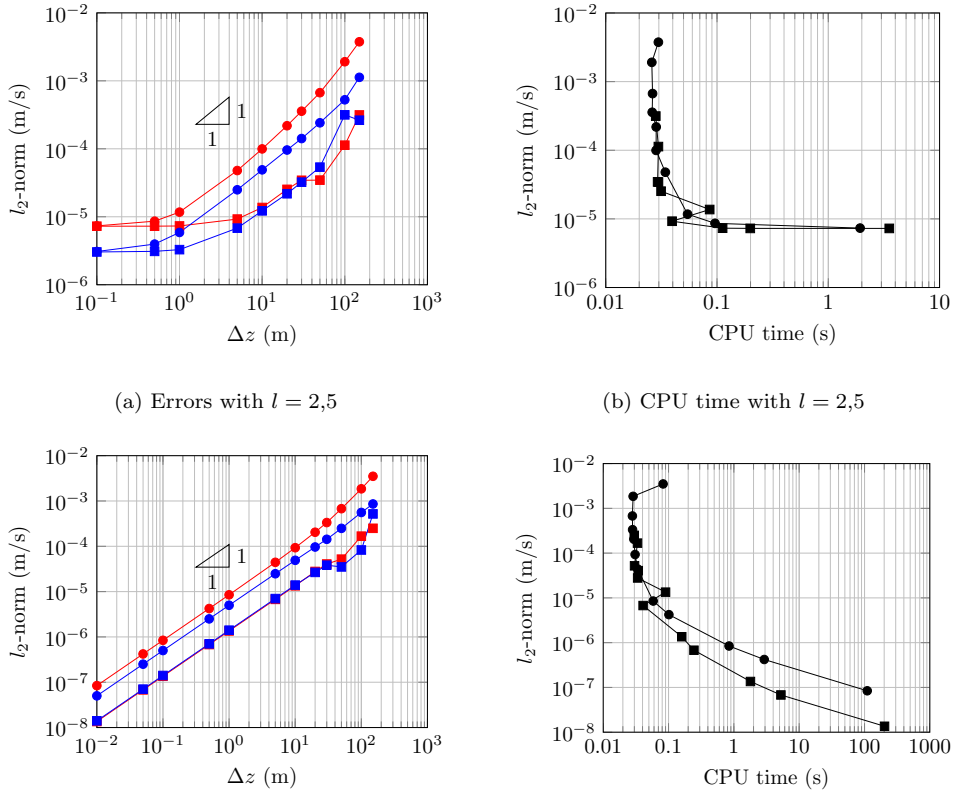

(a) Errors with $l = 2{,}5$

(b) CPU time with $l = 2{,}5$

(c) Errors with $l = 0{,}5$

(d) CPU time with $l = 0{,}5$

Figura A.13: Convergence plots at left for u (red) and v (blue), using SDS (dots) and CDS (squares). Computational time plots at right for SDS (dots) and CDS (squares).

For the condition *P-2*, inspired by Dritschel et al. (2020), a piecewise-constant eddy viscosity profile is proposed. It reads

$$K(z) = \begin{cases} \dfrac{\tau_0}{f\rho} & \text{if } z > z_h \\ l^2 \dfrac{\tau_0}{f\rho} & \text{if } z \leq z_h \end{cases} \tag{A.12}$$

where τ_0 is the magnitude of the surface wind stress and l is the ratio of the lower-layer to upper-layer viscous lengths (see values for l in Table 1). Note that the discontinuity in the diffusive flux is proportional to l^2. The results for the convergence rates with $l = 2{,}5$ are showed in Figure A.13a. The most striking result that emerge from the rates is that for CDS the order of accuracy drops from fourth to first. This loss of order is due to the oscillations of the solution around z_h, as is showed in Figure A.14. These oscillations are stemmed in the non-imposition of a jump condition on the derivative at z_h. SDS remains first order due the low resolution of the scheme at every grid point.

In spite of the fact this drawback, CDS shows a better performance than SDS. In the asymptotic range, $18,37\,\mathrm{m} \leq \Delta z \leq 225\,\mathrm{m}$, the errors for CDS in u and v components are similar whereas u is almost half-order worst than v in SDS. Finally, the l_2-norm of the error for CDS is below the SDS: one order in u and half order in v. In matter of CPU time, Figure A.13b displays the l_2-norm versus the CPU time. Results show both numerical schemes are comparable.

The results for the convergence rates for performance *P-2* with $l = 0{,}5$ are showed in Figure A.13c. Qualitatively, both numerical schemes display performances that remind to the ones observed in Figure A.13a. The asymptotic range covers a wide range of Δz instead of $l = 2{,}5$ and errors in both components of the velocity field match better each other for CDS.

Figure A.13d displays the l_2-norm versus the CPU time. Once it reaches the asymptotic range, lower the l_2-norm of the error quicker CDS from SDS is. For a norm of 10^{-7}, the CPU time in CDS is more than one decade faster than SDS.

Although in this paper the profile is continuous up to the first derivative (Equation (8)), it is unlikely to obtain some swing results as in the second condition.

Apéndice A.4. Numerical Model Performance

In performance *P-2*, an unexpected result was found for CDS, which lowers the accuracy of the scheme regarding that in condition *P-1*. Figure A.14 shows an incipient undesired behaviour that could amplify the oscillations if the mathematical model includes inertial terms. Nevertheless, there is ways to recover the accuracy and remove oscillations.

The exact solution derived by Dritschel et al. (2020) imposes the continuity of the diffusive flux at depth z_h where the two layers of eddy viscosity

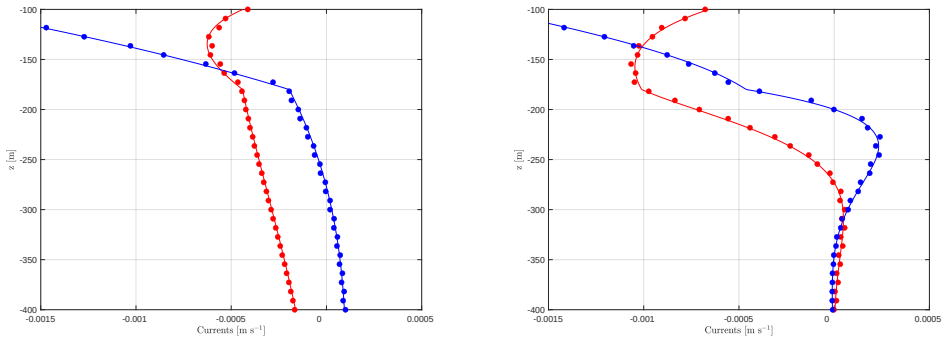

(a) Solutions with $l = 2{,}5$

(b) Solutions with $l = 0{,}5$

Figura A.14: Enlarged area for u (red dot) and v (blue dot) using CDS with the exact Dritschel solution for $u_{\text{Dritschel}}$ (red line) and $v_{\text{Dritschel}}$ (blue line).

are separated. In the numerical model, Equation (**??**), does not take this peculiarity into account by making these oscillations in Figure A.14. To guarantee this condition accurately, it must be ensured:

(I) Reach a jump condition in the diffusive flux at z_h but in the discrete sense. Note that Dritschel's paper obtains this condition by integrating the Ekman equation over an infinitesimal region centred at z_h, i.e. in the continuous sense.

(II) Separation of the two layers, z_h, does not have to be in a computational node. Guidelines should be considered to deal with interfaces (Li and Ito, 2006) and ensure good resolution (Feng et al., 2022).

Acknowledgements

VJL acknowledgments the financial support from Ministerio de Universidades and UniónEuropea-NextGenerationEU (Convocatoria de Recualificación Sistema Universitario Español−Convocatoria Complementaria "Margarita Salas"). EMP acknowledgments the financial support from the Plan Andaluz de Investigación, Desarrollo e Innovación (PAIDI 2020), funded by the European Union (Programa Operativo Fondo Social Europeo de Andalucía 2014-2020) and Junta de Andalucía. MDM would like to acknowledge support for this work from other research funding programs: EPICOS (Plan Andaluz de Investigación, Desarrollo e Innovación, PAIDI 2020. Ref. ProyExcel_00375) and DICHOSO (Proyectos de Generación de Conocimiento

2021 del Plan Estatal de Investigación Científica, Técnica y de Innovación 2021-2023. Ref. PID2021-125783OB-I00). Finally, the authors are grateful to Associate Editor Prof. Remi Tailleux and two anonymous reviewers for their comments, which helped to greatly improve the manuscript.

Code Availability

The results of this study can be reproduced using the free and open code available at the following URL: `https://github.com/GRANADA-gdfa/BETES`

Referencias

Basdurak, N.B., Burchard, H., Schuttelaars, H.M., 2021. A local eddy viscosity parameterization for wind-driven estuarine exchange flow. part i: Stratification dependence. Progress in Oceanography 193, 102548.

Berger, B., Grisogono, B., 1998. The Baroclinic, Variable Eddy Viscosity Ekman Layer. Boundary-Layer Meteorology 87, 363–380.

Bressan, A., Constantin, A., 2019. The deflection angle of surface ocean currents from the wind direction. Journal of Geophysical Research: Oceans 124, 7412–7420.

Burchard, H., 2002. Applied turbulence modelling in marine waters. volume 100. Springer Science & Business Media.

Chen, J., Qiao, W., Song, J., 2018. Numerical solution of unsteady Ekman equation modified by wave and linear friction term. Journal of Physics: Conference Series 1064, 012066.

Chen, W., de Swart, H.E., 2016. Dynamic links between shape of the eddy viscosity profile and the vertical structure of tidal current amplitude in bays and estuaries. Ocean Dynamics 66, 299–312.

Chereskin, T., 1995. Direct evidence for an Ekman balance in the california current. Journal of Geophysical Research: Oceans 100, 18261–18269.

Chkhetiani, O.G., Kurgansky, M.V., Vazaeva, N.V., 2018. Turbulent helicity in the atmospheric boundary layer. Boundary-Layer Meteorology 168, 361–385.

Chu, P.C., 2015. Ekman spiral in a horizontally inhomogeneous ocean with varying eddy viscosity. Pure and Applied Geophysics 172, 2831–2857.

Chu, P.C., Fan, C., 1999. A three-point sixth-order nonuniform combined compact difference scheme. Journal of Computational Physics 148, 663–674.

Constantin, A., 2021. Frictional effects in wind-driven ocean currents. Geophysical & Astrophysical Fluid Dynamics 115, 1–14.

Constantin, A., Johnson, R., 2019. Ekman-type solutions for shallow-water flows on a rotating sphere: A new perspective on a classical problem. Physics of Fluids 31, 021401.

Craig, P., Banner, M., 1994. Modeling wave-enhanced turbulence in the ocean surface layer. Journal of Physical Oceanography 24, 2546–2559.

Craig, P.D., 1989. Constant-eddy-viscosity models of vertical structure forced by periodic winds. Continental Shelf Research 9, 343–358.

Cronin, M.F., Kessler, W.S., 2009. Near-surface shear flow in the tropical pacific cold tongue front. Journal of Physical Oceanography 39, 1200–1215.

Cushman-Roisin, B., Deleersnijder, E., 2019. Top-to-bottom Ekman layer and its implications for shallow rotating flows. Enviromental Fluid Mechanics 19, 1105–1119.

Cushman-Roisin, B., Malačič, V., 1997. Bottom Ekman pumping with stress-dependent eddy viscosity. Journal of Physical Oceanography 27, 1967–1975.

Dobroklonskiy, S., 1969. Drift currents in sea with an exponentially decaying eddy viscosity coefficient. OCEANOLOGY-USSR 9, 19–+.

Dritschel, D.G., Paldor, N., Constantin, A., 2020. The Ekman spiral for piecewise-uniform viscosity. Ocean Science 16, 1089–1093.

Ekman, V.W., 1905. On the influence of the Earth's rotation on ocean-currents. Arkiv För Matematik, Astronomi Och Fysik. 2(11), 1–52.

Ezer, T., 2023. Evaluation of the applicability of the ekman theory for wind-driven ocean currents: a comparison with the mellor–yamada turbulent model. Ocean Dynamics 73, 575–591.

Feng, Q., Han, B., Peter Minev, P., 2022. A high order compact finite difference scheme for elliptic interface problems with discontinuous and high-contrast coefficients. Applied Mathematics and Computation 431, 127314.

Garvine, R.W., 1995. A dynamical system for classifying buoyant coastal discharges. Continental Shelf Research 15, 1585–1596.

Garvine, R.W., Monk, J.D., 1974. Frontal structure of a river plume. Journal of Geophysical Research 79, 2251–2259.

Grisogono, B., 1995. A generalized Ekman layer profile with gradually varying eddy diffusivities. Quarterly Journal of the Royal Meteorological Society 121, 445–453.

Guan, Y., Fečkan, M., Wang, J., 2022. Explicit solution of atmospheric Ekman flows with some types of Eddy viscosity. Monatshefte für Mathematik 197, 71–84.

Gula, J., Molemaker, M.J., McWilliams, J.C., 2014. Submesoscale cold filaments in the gulf stream. Journal of Physical Oceanography 44, 2617–2643.

Hansen, D.V., Rattray Jr, M., 1965. Gravitational circulation in straits and estuaries. Journal of Marine Research 23, 104–122.

Horner-Devine, A.R., Hetland, R.D., MacDonald, D.G., 2015. Mixing and transport in coastal river plumes. Annual Review of Fluid Mechanics 47, 569–594.

Ionescu-Kruse, D., 2021. Analytical atmospheric ekman-type solutions with height-dependent eddy viscosities. Journal of Mathematical Fluid Mechanics 23.

Jenkins, A.D., 1987. Wind and wave induced currents in a rotating sea with depth-varying eddy viscosity. Journal of Physical Oceanography 17, 938–951.

Kazantsev, C., Kazantsev, E., Blayo, E., 2003. Compact finite difference schemes for shallow-water ocean model. Technical Report RR-4913. INRIA. URL: https://hal.inria.fr/inria-00071667.

Lai, R.Y., Rao, D.B., 1976. Wind drift currents in deep sea with variable eddy viscosity. Archiv fuer Meteorologie, Geophysik und Bioklimatologie, Serie A 25, 131–140.

Lele, S.K., 1992. Compact finite difference schemes with spectral-like resolution. Journal of Computational Physics 103, 16–42.

Lenn, Y.D., Chereskin, T.K., 2009. Observations of Ekman currents in the southern ocean. Journal of Physical Oceanography 39, 768–779.

Lentz, S.J., 1995. Sensitivity of the inner-shelf circulation to the form of the eddy viscosity profile. Journal of Physical Oceanography 25, 19–28.

Lentz, S.J., Largier, J., 2006. The influence of wind forcing on the chesapeake bay buoyant coastal current. Journal of Physical Oceanography 36, 1305–1316.

Li, Z., Ito, K., 2006. The Immersed Interface Method: Numerical Solutions of PDEs Involving Interfaces and Irregular Domains. Society for Industrial and Applied Mathematics.

Lyons, T., 2021. Variable eddy viscosities in the atmospheric boundary layer from ageostrophic wind-speed profiles. Journal of Mathematical Fluid Mechanics 23.

Madsen, O.S., 1977. A realistic model of the wind-induced Ekman boundary layer. Journal of Physical Oceanography 7, 248–255.

McWilliams, J.C., Restrepo, J.M., 1999. Submesoscale cold filaments in the gulf stream. Journal of Physical Oceanography 29, 2523–2540.

Mellor, G., Blumberg, A., 2004. Wave breaking and ocean surface layer thermal response. Journal of Physical Oceanography 34, 693–698.

Mellor, G., Yamada, T., 1982. Development of a turbulence closure model for geophysical fluid problems. Reviews of Geophysics 20, 851–875.

Parmhed, O., Kos, I., Grisogono, B., 2005. An Improved Ekman Layer Approximation for Smooth Eddy Diffusivity Profiles. Boundary-Layer Meteorology 115, 399–407.

Price, J.F., Weller, R.A., Schudlich, R.R., 1987. Wind-driven ocean currents and Ekman transport. Science 238, 1534–1538.

Roberti, L., 2021. Perturbation analysis for the surface deflection angle of ekman-type flows with variable eddy viscosity. Journal of Mathematical Fluid Mechanics 23, 5.

Roberti, L., 2022. The Ekman spiral for piecewise-constant eddy viscosity. Applicable Analysis 101, 5528–5536.

Rosas-Villegas, F., Candela, J., Estrada-Allis, S., 2023. Eddy viscosity profiles and currents characterization of the bottom Ekman layer for the Western Gulf of Mexico continental shelf. Continental Shelf Research 254, 104906.

Rosas-Villegas, F., Candela, J., Ochoa, J., 2020. Eddy viscosity from bottom Ekman veering profiles. Continental Shelf Research 204, 104170.

Rossby, C.G., 1932. A generalization of the theory of the mixing length with applications to atmospheric and oceanic turbulence .

Shrira, V.I., Almelah, R.B., 2020. Upper-ocean Ekman current dynamics: A new perspective. Journal of Fluid Mechanics 887, 1–33.

Stewart, R.H., 2009. Introduction to Physical Oceanography. University Press of Florida.

Tan, Z., 2001. An Approximate Analytical Solution For The Baroclinic And Variable Eddy Diffusivity Semi-Geostrophic Ekman Boundary Layer. Boundary-Layer Meteorology 98, 361–385.

Taylor, J.R., Sarkar, S., 2008. Stratification effects in a bottom Ekman layer. Journal of Physical Oceanography 38, 2535–2555.

Taylor, J.R., Thompson, A.F., 2023. Submesoscale Dynamics in the Upper Ocean. Annual Review of Fluid Mechanics 55, 103–127.

Thomas, J.H., 1975. A theory of steady wind-driven currents in shallow water with variable eddy viscosity. Journal of physical oceanography 5, 136–142.

Welander, P., 1957. Wind action on a shallow sea: some generalizations of Ekman's theory. Tellus 9, 45–52.

Wenegrat, J.O., McPhaden, M.J., 2016a. A Simple Analytical Model of the Diurnal Ekman layer. Journal of Physical Oceanography 46, 2877–2894.

Wenegrat, J.O., McPhaden, M.J., 2016b. Wind, Waves, and Fronts: Frictional Effects in a Generalized Ekman Model. Journal of Physical Oceanography 46, 371–394.

Winant, C., Valle-Levinson, A., Ponte, A., Winant, C., Gutierrez-de Velasco, G., Winters, K., 2014. Observations on the lateral structure of wind-driven flows in a stratified, semiarid bay of the Gulf of California. Estuaries and Coasts 37, 1319–1328.

Witten, A.J., Thomas, J.H., 1976. Steady wind-driven currents in a large lake with depth-dependent eddy viscosity. Journal of Physical Oceanography 6, 85–92.

Wu, J., 1982. Wind-stress coefficients over sea surface from breeze to hurricane. Journal of Geophysical Research: Oceans 87, 9704–9706.

Yang, T., Fečkan, M., Wang, J., 2022. Atmospheric Ekman-type solutions with some eddy viscosities in ellipsoidal coordinates. Applicable Analysis , 1–14.

Yang, T., Fečkan, M., Wang, J., 2023. Explicit solutions of atmospheric Ekman flows for some eddy viscosities in ellipsoidal coordinates. Dynamics of Partial Differential Equations 20, 99–115.

Yoshikawa, Y., Endoh, T., 2015. Estimating the eddy viscosity profile from velocity spirals in the Ekman boundary layer. Journal of Atmospheric and Oceanic Technology 32, 793–804.